materials

MDPI

Review

Review and New Perspectives on Non-Layered Manganese Compounds as Electrode Material for Sodium-Ion Batteries

Ricardo Alcántara [1,*], Carlos Pérez-Vicente [1], Pedro Lavela [1], José L. Tirado [1], Alejandro Medina [1] and Radostina Stoyanova [2]

[1] Department of Inorganic Chemistry, Institute of Chemistry for Energy and Environment (IQUEMA), Faculty of Sciences, Campus of Rabanales, University of Cordoba, Building Marie Curie, 14071 Córdoba, Spain; iq3pevic@uco.es (C.P.-V.); iq1lacap@uco.es (P.L.); iq1ticoj@uco.es (J.L.T.); q42mejaa@uco.es (A.M.)

[2] Institute of General and Inorganic Chemistry, Bulgarian Academy of Sciences, 1113 Sofia, Bulgaria; radstoy@svr.igic.bas.bg

* Correspondence: ralcantara@uco.es

Abstract: After more than 30 years of delay compared to lithium-ion batteries, sodium analogs are now emerging in the market. This is a result of the concerns regarding sustainability and production costs of the former, as well as issues related to safety and toxicity. Electrode materials for the new sodium-ion batteries may contain available and sustainable elements such as sodium itself, as well as iron or manganese, while eliminating the common cobalt cathode compounds and copper anode current collectors for lithium-ion batteries. The multiple oxidation states, abundance, and availability of manganese favor its use, as it was shown early on for primary batteries. Regarding structural considerations, an extraordinarily successful group of cathode materials are layered oxides of sodium, and transition metals, with manganese being the major component. However, other technologies point towards Prussian blue analogs, NASICON-related phosphates, and fluorophosphates. The role of manganese in these structural families and other oxide or halide compounds has until now not been fully explored. In this direction, the present review paper deals with the different Mn-containing solids with a non-layered structure already evaluated. The study aims to systematize the current knowledge on this topic and highlight new possibilities for further study, such as the concept of entatic state applied to electrodes.

Keywords: post-lithium batteries; sodium-ion batteries; spinel; phosphate; multianion; manganese compounds

check for updates

Citation: Alcántara, R.; Pérez-Vicente, C.; Lavela, P.; Tirado, J.L.; Medina, A.; Stoyanova, R. Review and New Perspectives on Non-Layered Manganese Compounds as Electrode Material for Sodium-Ion Batteries. *Materials* **2023**, *16*, 6970. https://doi.org/10.3390/ma16216970

Academic Editor: Alessandro Dell'Era

Received: 13 September 2023
Revised: 13 October 2023
Accepted: 22 October 2023
Published: 30 October 2023

1. Introduction

Rechargeable batteries for renewable energy storage should be made from abundant, inexpensive, and low-toxicity elements. The production of lithium-ion batteries could be limited mainly due to the scarcity of mineral reserves and the high cost of lithium and other elements such as cobalt, nickel, and copper (Figure 1) [1,2]. Therefore, abundant, and cheap materials for sustainable batteries are being intensively investigated. SIB could be competitive against LIB, particularly in terms of economic cost and abundance of mineral resources. Another advantage is that aluminum could be used as a current collector for both the positive and the negative electrode because Na does not alloy with Al, avoiding Cu. In addition, SIB can be particularly useful for large-scale energy storage.

Unfortunately, the larger size of Na^+ compared to Li^+ (1.02 vs. 0.69 Å) could be a disadvantage, and the accommodation and mobility of sodium into the host material can be difficult. The structural changes induced by the intercalation and deintercalation of sodium can deteriorate the crystal structure and lead to battery failure. Thus, finding the most suitable materials for SIB is a great challenge.

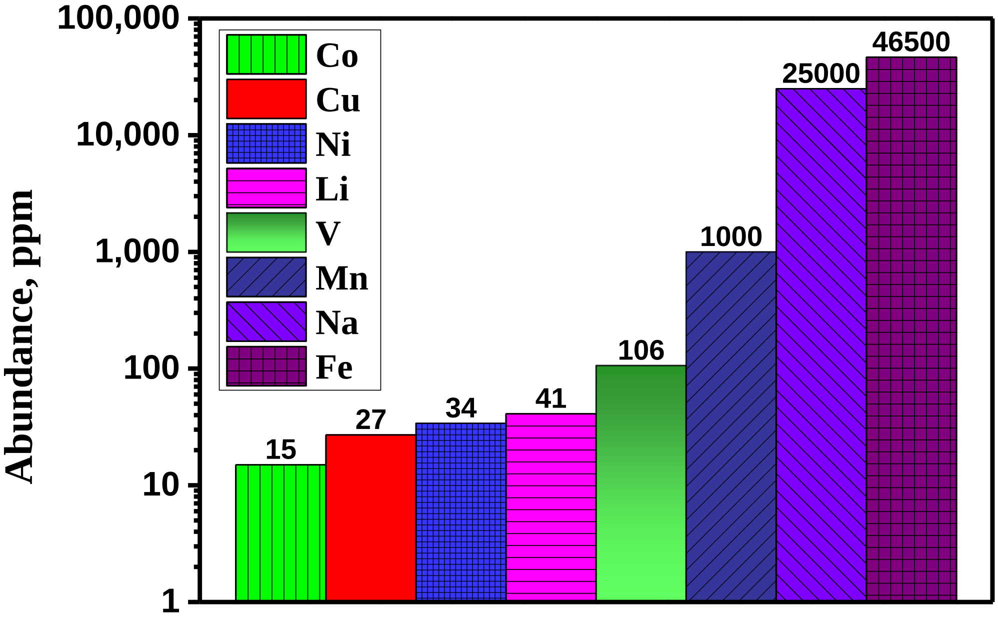

Figure 1. Element abundances of the upper continental crust [1,2].

Manganese is particularly interesting as the main component of the electrode active material, because of its low cost, natural abundance (Figure 1), and low toxicity, compared to other elements such as nickel and cobalt. Early investigations unveiled the existence of several phases in the Na_xMnO_2 system ($0 < x < 1$) in which sodium ions can be (de)intercalated [3,4]. Thus, several manganese oxides are promising as electrode-active materials for SIB, including 3D and 2D structures. Another advantage could be the diversity of oxidation states of Mn, which could help deliver high capacity. The study and selection of the most adequate structures are key for developing high-performance electrodes for non-aqueous sodium-ion batteries. A main challenge for using some manganese oxides, such as the spinel-type compound AMn_2O_4, is the instability of the crystal structure because the structural change can drive battery failure. Many layered oxides (2D structures) are often incapable of accommodating the structural change and the strains due to the Jahn–Teller effect of Mn(III) ion during the charge/discharge of the battery.

The low cost, natural abundance, and sustainability of sodium and manganese elements are the main justifications for the interest in these materials. Although we have learnt a lot from LIBs, SIBs are still more challenging, and great efforts are still needed. The layered-type oxides are not included in this review, except for the heterostructured materials, because the layered-type materials have been extensively investigated and the great number of papers published on this subject would deserve another review paper. A main disadvantage of the layered-type materials is that often they suffer structure transformation and poor cycling stability. Some non-layered materials could be competitive in terms of cycling stability. The main goal of this article is to review the main properties of these materials, their advantages and disadvantages, and the challenges and possible ways to advance in this field. This review first focuses on Mn-based oxides with spinel-type structures and other structures related to that such as tunneled-type, and post-spinel, which are employed as intercalation electrode material in non-aqueous sodium-ion batteries. Secondly, manganese fluorides and oxyfluorides are reviewed. Thirdly, the most relevant manganese-based multianion compounds, such as phosphates, carbonates, and silicates, are also included. Finally, the conversion electrode materials are reviewed. The classification of these types of materials is schematized in Figure 2, and the main properties of the materials are summarized in Table 1.

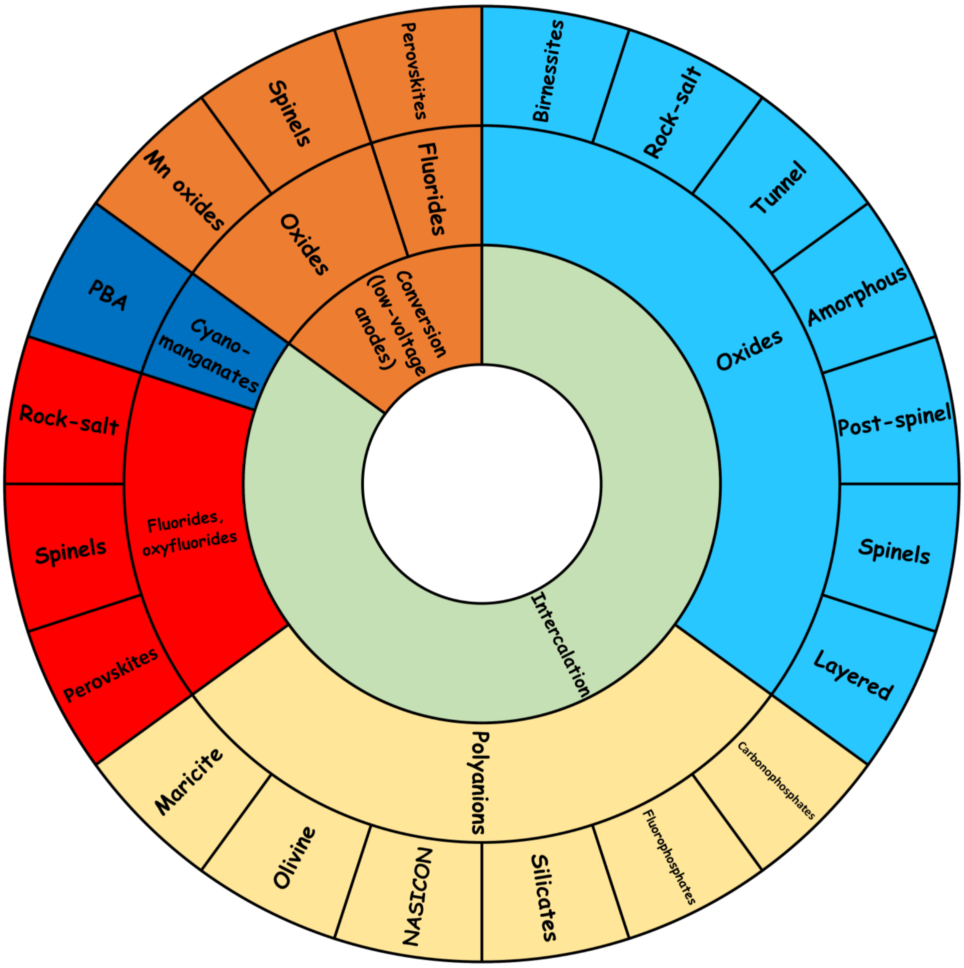

Figure 2. Schematic overview of the main types of Mn-based materials for SIB.

Table 1. Summary of the relevant Mn-based materials with the non-layered structure for sodium intercalation. Voltage range and capacity values are taken from the experimental results reported in the references.

Electrode Material (Structure Type)	Space Group	Voltage Range, V	Capacity, mAh g^{-1}	Refs.
λ-MnO_2 (spinel)	Fd-3m	2.0–4.0	180	[6]
$Mn_{2.2}Co_{0.27}O_4$ (tetragonal spinel)	$I4_1/amd$	1.5–4.0 V	95	[7]
$LiMn_2O_4$ (cubic spinel)	Fd-3m	2.0–4.0	190	[11]
$Li_{1.2}Mn_{1.8}O_4$ (cubic spinel)	Fd-3m	2.0–4.0	65	[11]
$NaMn_2O_4$ ($CaFe_2O_4$ post-spinel)	Pnma	1.6–4.8	80	[20]
$Na_{0.9}MnSnO_4$ ($CaFe_2O_4$ post-spinel)	Pnma	2.0–4.5	30	[21]
$NaMn_2O_4$ (cubic spinel)/Na_xMnO_2 (layered)	Fd-3m	2.2–3.6	181	[12]
$Li_{2-x}MnO_3$ (cubic spinel)	Fd-3m	1.5–4.2	160–200	[13]
$Na_{0.44}MnO_2$ (tunnel)	Pbam	2.0–4.0	140	[23]
$Na_{0.44}Mn_{1-x}Ti_xO_2$	Pbam	1.5–3.8	100–110	[29]
$Na_{0.44}Mn_{0.89}Ti_{0.11}O_2$	Pbam	2.0–4.0	71–119	[30]
$Na_{0.61}[Mn_{0.27}Fe_{0.34}Ti_{0.39}]O_2$	Pbam	2.6–4.2	98	[32]
$Na_{0.44}Mn_{0.9925}Co_{0.0075}O_2$	Pbam	2.0–4.0	138	[33]

Table 1. *Cont.*

Electrode Material (Structure Type)	Space Group	Voltage Range, V	Capacity, mAh g^{-1}	Refs.
$Na_{0.44}MnO_2$ (tunnel)/$LiMn_2O_4$ (cubic spinel)	Pbam/Fd3m	2.0–4.0	120	[24]
$Na_{0.44}MnO_2$ (tunnel)/$Na_2Mn_3O_7$(layered)	$Pmc2_1$	1.5–4.7	145–278	[26]
$Na_{0.44}Mn_{0.97}Al_{0.01}Ti_{0.01}Co_{0.01}O_2$ (tunnel)	Pbam	2.0–4.0	140	[52]
$Ni_{0.5}Mn_{1.5}O_4$ (cubic spinel)	Fd-3m	2.5–4.7	140	[66]
$NaMnO_2$ (disordered rocksalt)	Fm-3m	1.2–4.5	200	[59]
$Na_{1.3}Nb_{0.3}Mn_{0.4}O_2$ (disordered rocksalt)	Fm-3m	1.0–4.0	150–200	[70]
$Na_{1.14}Mn_{0.57}Ti_{0.29}O_2$ (disordered rocksalt)	Fm-3m	1.2–4.5	200	[71]
Na_2MnO_2F (disordered rocksalt)	Fm-3m	1.5–4.5	220	[83]
Na_2MnF_5	$P2_1/c$	1.0–4.7	ca. 0	[81]
$NaMnF_3$ (perovskite)	Pnma	2.0–4.3	89	[82]
$K_{0.97}Ni_{0.31}Zn_{0.28}Mn_{0.41}F_{2.84}$@rGO (composite of perovskite and graphene)	Pm-3m	0–3	173	[163]
$K_{0.86}MnF_{2.69}$@rGO (composite of perovskite and graphene)	Pm-3m	0–3	40	[161]
$Li_{1.1}Mn_{1.5}Ni_{0.5}O_{3.8}F_{0.2}$ (cubic spinel)	Fd-3m	2.5–4.7	140	[66]
$Li_4Mn_5O_{12}$ (cubic spinel)	Fd-3m	2.3–3.3	140	[73]
$Mg_{0.3}Mn_2O_4$ (cubic spinel)	Fd-3m	1.5–4.4	90–105	[15]
$Mg_{0.8}Mn_{1.9}Fe_{0.1}O_4$ (tetragonal spinel)	$I4_1/amd$	1.5–4.4	70	[15]
α-MnO_2 (hollandite)	I4/m	1.0–4.0	109	[54]
α-$Ag_{1.22}Mn_8O_{16}$ (hollandite)	I4/m	1.3–3.8	247	[62]
β-MnO_2	$P4_2/mnm$	1.0–4.3	264–280	[64]
MnO_2 (amorphous)	-	1.5–4.0	139	[65]
$NaMnPO_4$ Mg-doped (olivine)	Pmnb	2.1–4.6	100	[87]
$NaMnPO_4$ (maricite)	Pnma	1.5–4.5	102	[90]
$Na_3MnCO_3PO_4$	P21/m	2.0–4.5	177	[101]
Na_2MnSiO_4	Pn	2.0–4.3	210	[122]
$Na_4MnV(PO_4)_3$ (NASICON)	R-3c	2.5–3.8	112.3	[118]
$Na_3MnTi(PO_4)_3$ (NASICON)	R-3c	2.4–4.2	114	[112]
$Na_3MnZr(PO_4)_3$ (NASICON)	R-3c	2.5–4.3	105	[111]
Na_2MnPO_4F	$P2_1/n$	1.5–4.5	102.4	[96]
$Na_2Fe_{0.5}Mn_{0.5}PO_4F$	$P2_1/n$	2.0–4.5	107	[95]
$Na_2Mn[Mn(CN)_6]$ (Prussian blue analog)	$P2_1/n$	1.3–4.0	209	[128]
Mn_3O_4	$I4_1/amd$	0.0–3.0	100–250	[155]
Mn_2O_3	Ia-3	0.0–3.0	100–210	[156]
γ-MnOOH	P21/c	0.005–2.8	300–421	[157]
$MnFe_2O_4$@C (cubic spinel and carbon nanofibers)	Fd-3m	0.0–3.0	305	[159]
$MnFe_2O_4$@rGO (cubic spinel and graphene)	Fd-3m	0.0–3.0	258	[158]
$CoMn_2O_4$ (spinel)	Fd-3m	0–2.5	185–347	[160]

2. Manganese Oxides for Sodium Intercalation

For the intercalation of sodium into manganese oxides at voltages over ca. 2 V vs. Na^+/Na, compounds with a variety of structures have been studied, such as spinel, post-spinel, tunnel, and rock salt, and these compounds are reviewed below.

2.1. Spinel-Type $NaMn_2O_4$

The synthesis of spinel-type $NaMn_2O_4$ using the conventional solid-state method is impossible. Tarascon et al. obtained cubic λ-MnO_2 (Figure 3) by following the procedure reported by Hunter, which is based on the delithiation of the spinel-type $LiMn_2O_4$ by acid-leaching or by chemical oxidation, and then they found that the electrochemical insertion of sodium into λ-MnO_2 drives the migration of manganese atoms in the oxide framework and structure transformation from spinel-type to layered-type Na_xMnO_2 (with $\Delta x = 0.6$) [5,6].

As an alternative to cubic λ-MnO_2, Bach et al. employed the tetragonal spinel $Mn_{2.2}Co_{0.27}O_4$ [7]. Up to one Na per formula unit ($NaMn_{2.2}Co_{0.27}O_4$) can reversibly intercalate in the 3D structure. However, the capacity retention was not particularly good, and around 0.67–0.5 Na intercalated after 10 cycles.

It is generally accepted that the spinel-type $NaMn_2O_4$, with 3D channels for Na-diffusion, is not thermodynamically stable [8,9]. Thus, the spinel transforms into the layered form of $NaMn_2O_4$ after a few cycles in a sodium battery. Inversely, the spinel $LiMn_2O_4$ is more stable than the layered form of $Li_{0.5}MnO_2$, and the spontaneous transformation of the layered structure into a spinel structure was observed during cycling in lithium batteries [10]. This is related to the higher energy barrier for manganese migration and cation mixing in the oxide packing of layered O3 $Na_{0.5}MnO_2$ compared to $Li_{0.5}MnO_2$, because manganese migration involves a difficult displacement of sodium to the tetrahedral site.

Yabuuchi et al. confirmed that the electrochemical delithiation and then sodium insertion into stoichiometric $LiMn_2O_4$ (s.g. Fd-3m) induce a phase transition to layered $NaMnO_2$. This layered $NaMnO_2$ exhibits relatively good capacity retention and ca. 130 mAh g^{-1} of capacity for a voltage range between 3.0 and 4.3 V, and the capacity is higher (190 mAh g^{-1}), but the retention is poorer for the 2.3–4.3 V voltage range. They also reported that the intercalation of sodium into non-stoichiometric spinel-type $Li[Li_{0.2}Mn_{1.8}]O_4$ induces strain in the crystal lattice and the phase transition into the layered phase was not observed [11].

Tang et al. delithiated the spinel-type $LiMn_2O_4$ by charging up to 4.3 vs. Li^+/Li, and then sodiated the resulting manganese oxide by discharging down to 2.0 V vs. Na^+/Na [12]. The resulting sample is a mixture of spinel-type $NaMn_2O_4$ and layered $Na_xMn_2O_4$ with a small amount of residual lithium. Interestingly, the in situ formed layered structure appears as a shell surrounding the core spinel structure in a single particle forming and intergrowth structure. In this spinel-layered intergrowth structure, the layered phase would be the main phase for the reversible intercalation of sodium, while the spinel phase would stabilize the electrode material during the charge/discharge process.

Instead of using $LiMn_2O_4$, Kataoka et al. first prepared monoclinic layered $Li_2Mn_2O_3$ (s.g. C2/m) as a precursor [13]. Secondly, they obtained $Li_{2-x}MnO_3$ with cubic spinel structure (s.g. Fd-3m) by electrochemical delithiation of $Li_2Mn_2O_3$ and rinsing several times with dimethyl carbonate solvent. Finally, they used the resulting delithiated manganese oxide with x = 1.6–1.8 in a sodium cell, with an experimental capacity of around 160–200 mAh g^{-1}. The resulting electrode material retains the spinel structure during sodiation/desodiation cycles, and they suggested that the migration of Mn to the tetrahedral sites is more energetically unfavorable than for the lithiated compound, due to the difference in ionic radii, and the cycle stability can be better in sodium than lithium cell. In addition, they pointed out that the structure of this spinel $NaMnO_2$ is tetragonally distorted (Figure 3).

For the AMn_2O_4 spinel (A = Li, Na or Mg), Kolli and Van der Ven assumed that small cations (Li^+ and Mg^{2+}) prefer to occupy the tetrahedral site, while larger Na^+ prefers to occupy the octahedral site (16c) [14]. Recent theoretical calculations on the intercalation of sodium into λ-MnO_2 unveiled that initially the occupation of the tetrahedral site by sodium is energetically more favorable than the octahedral site for the composition $Na_{0.125}Mn_2O_4$ [15]. The calculated insertion voltage is 2.85 V, and the lattice cell would expand upon sodium intercalation. On the other hand, this result does not involve that the sodiated spinel is thermodynamically stable, and in fact, it is known that more sodiation yields the layered structure. In fact, the structural transformation of the spinel can be detrimental to the electrochemical cycling.

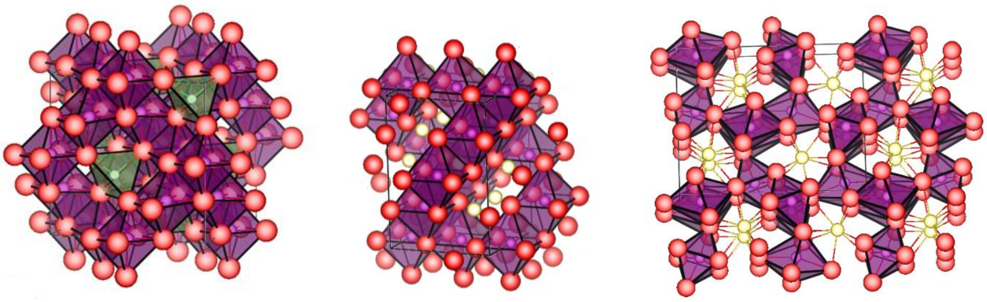

(a) $Li_{0.03}Mn_2O_4$ Fd-3m

(b) $NaMnO_2$ $I4_1/amd$

(c) $NaMn_2O_4$ Pnma

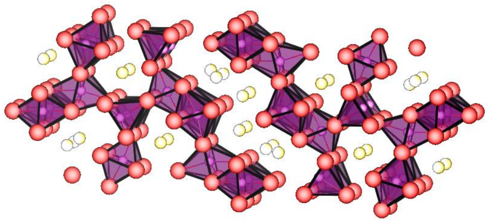

(d) $Na_{0.44}MnO_2$ Pbam

Figure 3. Structures of several Mn-containing electrode materials. (**a**) Cubic spinel $Li_{0.03}Mn_2O_4$ [16]. (**b**) Tetragonal spinel $NaMnO_2$ [13]. (**c**) $NaMn_2O_4$ [17]. (**d**) Tunnel-type, $Na_{0.44}MnO_2$ [18].

2.2. Calcium Ferrite-Type $NaMn_2O_4$

In 2006, Yamamura et al. reported that the spinel-type structure of $LiMn_2O_4$ can be transformed into the $CaFe_2O_4$-type by heating under 6 GPa of pressure, and thus a new form of $LiMn_2O_4$ was obtained [19]. This calcium ferrite structure is about 6% denser than the spinel, all the Mn are in a 6-fold coordination by oxygen, and the MnO_6 forms a double chain-type unit.

Analogously to $LiMn_2O_4$, the so-called "post-spinel" $NaMn_2O_4$, with $CaFe_2O_4$-type structure and s.g. Pnma was first obtained by the structural transformation of spinel $NaMn_2O_4$ under high pressure by Akimoto et al. [17] (Figure 3). The MnO_6 octahedra share edges and form 1D tunnels for easy sodium diffusion. In contrast to the spinel-type $NaMn_2O_4$, the post-spinel $NaMn_2O_4$ is thermodynamically stable. The high energy barrier of the rearrangement of the MnO_6 octahedron suppresses the Jahn–Teller distortion in the post-spinel $NaMn_2O_4$. Unfortunately, the reinsertion of sodium is very difficult, particularly for large particles [20].

The post-spinel type $NaMnSnO_4$ (s.g. Pnma), in which tin atoms stabilize the structure, can be synthesized at ambient pressure [21]. The reversible capacity of this material in a sodium cell was only about 25–30 mAh g^{-1} in the range between 2.0 and 4.5 V, and the XRD patterns do not show significant changes during sodium (de)intercalation.

2.3. Tunnel-Type $Na_{0.44}MnO_2$

Doeff et al. first reported the use of orthorhombic Na_xMnO_2 with x = 0.44 and 0.2 as the cathode of a sodium battery at 85 °C and they employed poly(ethylene oxide) and $NaCF_3SO_3$ in the polymer electrolyte [22]. They treated the compound $Na_{0.44}MnO_2$ with aqueous hydrochloric acid for its partial desodiation from x = 0.44 to 0.2. Later, Sauvage et al. prepared single-phase $Na_4Mn_9O_{18}$ (or $Na_{0.44}MnO_2$) and provided a detailed structure characterization [23]. This oxide has an orthorhombic tunnel-type structure (s.g. Pbam) with two types of tunnels: a small tunnel and an S-shaped large tunnel. MnO_6 and MnO_5 polyhedrons form S-shaped tunnels, which are very suitable for sodium diffusion [23,24] (Figure 2). According to theoretical calculations, there are three sites for sodium (Na1, Na2, and Na3) [25]. The small tunnel is almost filled by Na1. A large S-shaped tunnel is half-filled by Na2 (trigonal prismatic coordination) and Na3. Due to the Jahn–Teller distortion of Mn^{3+}, the change of the lattice cell parameters in crystallographic directions of the b-axis and c-axis is anisotropic. Interestingly, the transformation to the spinel-type structure does not occur due to a size mismatch between Na and Mn and different oxygen frameworks. The maximum capacity is 140 mAh g^{-1}, and the system Na_xMnO_2 is fully reversible for $0.25 < x < 0.65$ within the voltage range between 2.0 and 3.8 V (Figure 4) [23,25]. However, there is partial irreversibility for $x < 0.25$. The Jahn–Teller effect, the presence of several biphasic transitions, and the dissolution of Mn(II) ions into the electrolyte solution can be the main reasons for the poor capacity retention. If the amount of sodium is higher than $x > 0.44$, a layered structure may form.

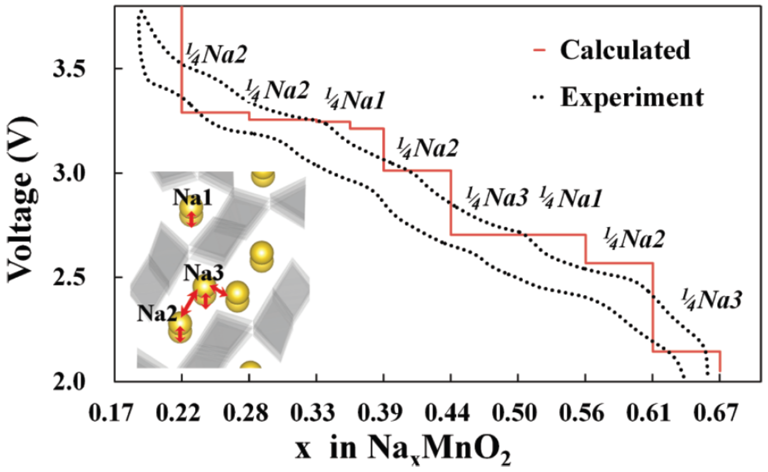

Figure 4. Calculated and experimental voltage profile of tunnel-type Na_xMnO_2 in sodium cell. Reprinted (adapted) with permission from Ref. [25]. Copyright (2012) ACS.

A mixture between Mn(III) and Mn(IV) oxidation states is expected in $Na_{0.44}MnO_2$. Replacing the Jahn–Teller ion Mn(III) with a non-Jahn–Teller ion (Mn(IV)) can improve the cyclability [26,27]. Another strategy proposed by Liang et al. is Li-doping and the formation of a $Na_{0.44}MnO_2/LiMn_2O_4$ heterostructure [24]. The lithium ions in the heterostructure function as pillars to stabilize the structure.

Partial replacement of Mn by other transition metals is an explored strategy to enhance the electrochemical performance. Doping sodium manganate opens different opportunities. Ti-substituted $Na_{0.44}Mn_{1-x}Ti_xO_2$ also has a tunnel-type structure and has been a proposed electrode for both aqueous and non-aqueous sodium-ion batteries [28,29]. The incorporation of Ti results in an expansion of the unit cell volume. During the charge/discharge cycling, the composition changes between $Na_{0.22}Mn_{1-x}Ti_xO_2$ and $Na_{0.66}Mn_{1-x}Ti_xO_2$. Multiple plateaus appear in the voltage curve for Na_yMnO_2, while a sloping profile is observed for Ti-doped samples, which is typical of a solid solution. The disordered Mn/Ti arrangement could break the ordering in $Na_{0.66}Mn_{1-x}Ti_xO_2$ during the (de)intercalation of sodium. After the incorporation of Ti, the tunnel structure remains preserved even for higher Na-content, and the capacity retention is improved [30]. Similarly, according to Jia et al., Ti-doping particularly stabilizes the tunnel structure for $Na_{0.66}Mn_{0.9}M_{0.1}O_{2+\delta}$ (M = dopant), the Ti-doped sample operates at higher voltage, and the observed hysteresis in the voltage curve minimizes [31].

Iron is another cheap and abundant element that could be employed in electrodes. The structure of $Na_{0.61}[Mn_{0.61-x}Fe_xTi_{0.39}]O_2$ is also tunnel-type. and these compounds are particularly air-stable [32]. According to XANES and ^{57}Fe Mössbauer results, during the charge/discharge process, the oxidation state of manganese and iron (Fe^{3+}/Fe^{4+}) take part in the charge compensation, while the oxidation state of titanium remains unchanged. The participation of the iron redox couple provides a high average voltage (3.56 V).

For stabilization of the tunnel structure and preventing the transformation to a layer-type structure after cobalt-doping, it is necessary to keep the mole ratio Co/Mn under 0.01. For example, Zhong et al. studied $Na_{0.44}Mn_{0.9925}Co_{0.0075}O_2$ [33]. Since Co^{3+} is smaller than Mn^{3+}, the MO_5 and MO_6 polyhedra contract, the S-shape tunnel is enlarged, and sodium mobility is easier. In addition, Co-doping improves the electronic conductivity and structural stability, and it could suppress the Mn dissolution. The incorporation of aluminum in $Na_{0.44}MnO_2$ drives a mixture between tunnel-type $Na_{0.44}MnO_2$ and orthorhombic layered-type $NaAl_{0.1}Mn_{0.9}O_2$ [34]. The Al-O bonds in the surface of the particles contribute to improving the electrode stability.

Control of the particle size and morphology can be another strategy to improve the charge/discharge rate and stability of $Na_{0.44}MnO_2$ [35–37]. For that purpose, Dai et al. employed a synthesis method based on the combustion of PVP and obtained rod-shaped particles [37]. The resulting diffusion coefficient of sodium was between 1.5×10^{-12} cm^2 s^{-1} and 2.7×10^{-10} cm^2 s^{-1}, depending on the charge state, such as lithium in $LiMn_2O_4$. The maximum capacity value was 123 mAh g^{-1} at C/5. The direction [001] (parallel to the c-axis) is the favorite direction for the crystal growth in $Na_{0.44}MnO_2$ and then particles with nanorod morphology are easily prepared [38]. Nevertheless, the particles with nanoplate shape, which exhibit more particle surface perpendicular to the c-axis, reduce the distance of the more difficult pathway for sodium diffusion, and it can drive to a better rate capability. The reduction of the crystal growth in the [001] direction can provide outstanding high-rate capability (96 mAh g^{-1} at 10C) and remarkable cycling stability. Multiangular rod-shaped particles were prepared by using the reverse microemulsion method, and this material possesses very stable cycling performance (99.6% capacity retention after 2000 cycles), although the capacity is low (Figure 5) [36].

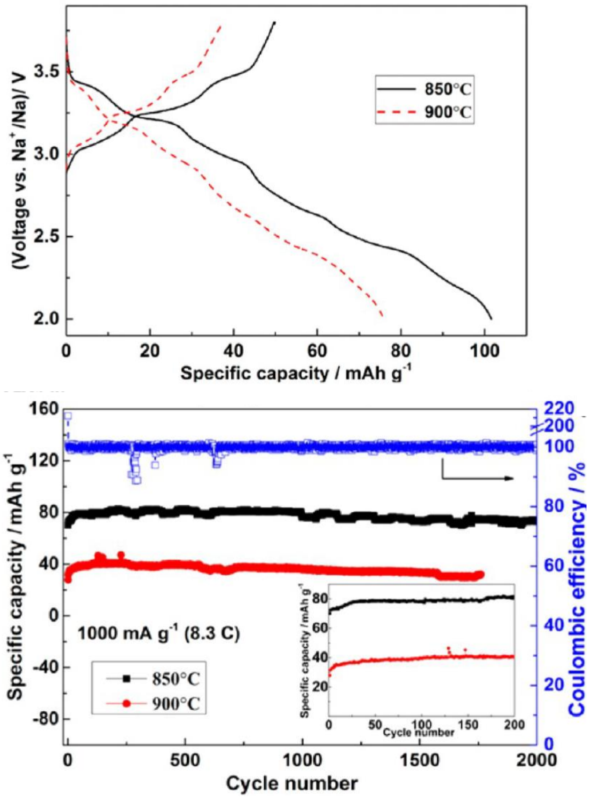

Figure 5. Electrochemical properties of multiangular rod-shaped $Na_{0.44}MnO_2$ in a sodium cell. Reprinted (adapted) with permission from Ref. [36]. Copyright (2017) ACS.

A green battery can be eco-friendly and developed with $Na_{0.44}MnO_2$ as a cathode, hard carbon as an anode, and CMC as a binder [39]. This CMC binder is low cost, not toxic, and it can be employed through aqueous processing, which improves sustainability and decreases the environmental impact of the battery technology, compared to processing with organic solvents. Interestingly, $Na_{0.44}MnO_2$ is sufficiently stable for aqueous processing. On the other hand, the hard carbon must be presodiated to compensate for its initial irreversible consumption of sodium, thus avoiding employing an excess of $Na_{0.44}MnO_2$. Another way to counteract the sodium deficiency of this cathode avoiding anode presodiation is by blending a sacrificing additive in the cathode, for example, pentasodium diethylenetriaminepentaacetate [40]. The urea-based solution combustion synthesis can be an eco-friendly route to obtain $Na_{0.44}MnO_2$ [41].

A multifunctional effect of Na_2MoO_4 is that a surface layer of this molybdate protects the electrode material from the attack of HF in the electrolyte and facilitates electron transfer. Electroconducting nanolayers of Na_2MoO_4 autogenously form on the surface of $Na_{0.44}MnO_2$ particles, driving superior electrode performance [42]. These surface layers gradually transformed into MoF_6 and MoO_2F_2 layers in the presence of HF.

It is worth noting that part of the sodium atoms can vaporize during the ceramic synthesis of the sodium manganates, and an excess of sodium (typically 5%) is employed in many syntheses. Thus, it is not easy to control the final Na/Mn ratio and stoichiometry [43]. According to recent DFT calculations, vacancies and defects greatly impact the electrochemical performance of $Na_{0.44}MnO_2$ [44]. Oxygen vacancies decrease the (de)intercalation voltage, while Mn vacancies increase the voltage, and defects improve sodium diffusivity.

While the compounds Na_xMnO_2 with $0.22 \leq x \leq 0.44$ possess a tunnel-type structure, a mixture between tunneled and layered structures is obtained for $0.66 < x \leq 1.0$. The tunneled compound has a limited capacity, while the layered form has a larger capacity but poorer cycling stability. The layered compound $Na_2Mn_3O_7$, with a triclinic structure, can deliver higher voltage (up to 4.7 V), and the oxygen redox contributes to an exceptionally large capacity (250 mAh g^{-1}) [45–49]. However, the stability of the oxygen redox processes is not particularly good. To enhance the electrochemical behavior, Zheng et al. proposed to employ the $Na_{0.44}MnO_2/Na_2Mn_3O_7$ heterojunction material [50]. The pillar function of tunnel-type $Na_{0.44}MnO_2$ improves the coulombic efficiency and cycling stability of $Na_2Mn_3O_7$. Thus, the heterojunction could be a valid strategy.

Magnesium-doping is another strategy to stabilize the tunnel structure, although too much Mg forms the layered structure. Thus, $Na_{0.44}Mn_{0.95}Mg_{0.05}O_2$ exhibits lower voltage polarization and superior long-cycle stability [51]. This may be because the Mg-doping facilitates sodium mobility and increases the electrons near the Femi level. A very new strategy to improve the rate capability and cycling stability is the medium-entropy substitution of tunnel-type sodium manganate—$Na_{0.44}Mn_{0.97}Al_{0.01}Ti_{0.01}Co_{0.01}O_2$ [52].

Tevar et al. reported that the materials made with a solid-state synthesis and Na:Mn precursor ratio equal to 0.55 contained $Na_{0.44}MnO_2$, as well β-$Na_{0.70}MnO_2$ and α-Mn_2O_3 minor impurity phases [43]. According to Zhang et al., the sodium-rich compound $Na_{0.6}MnO_2$ can be prepared with a slightly different and novel structure also possessing S-tunnel, and they indexed the XRD pattern to an orthorhombic lattice [53]. This material can be prepared with the aid of the surfactant CTAB, and it delivers higher capacity and superior cycling stability. In contrast, the CTAB-free $Na_{0.6}MnO_2$ material is a mixture of tunnel and layer structures and it presents less charge capacity due to the lower amount of sodium in $Na_{0.44}MnO_2$ compared to CTAB-$Na_{0.6}MnO_2$. The guidance of the CTAB surfactant helps to form the Na-rich particles with rod-shaped morphology.

2.4. Tunnel-Type MnO_2

The manganese oxide polymorph α-MnO_2 (hollandite-type) possesses a tetragonal 1D structure (s.g. I4/m) with tunnels (Figure 6), and it can be prepared with nanorods and nanoflowers morphology through hydrothermal method [54,55]. The sodium ions can diffuse easily through the open channels. A higher capacity for $NaClO_4$/PC-FEC electrolyte than $NaPF_6$/EC-DMC-FEC electrolyte was observable, but the capacity fading is severe in $NaClO_4$/PC-FEC and at high current density, and this might be due to the decomposition of PC on the MnO_2 particle surface and the consequent cell polarization. The additive (typically 5%) fluoroethylene carbonate (FEC) forms a stable SEI film and improves the efficiency and stability of the Na cell, but it introduces polarization. The theoretically calculated insertion voltage is 3.42 [54] or 3.23 V [56], but the experimental voltage range is 1.0–40 V. The calculated diffusion barrier energy is as low as 0.21 eV, and sodium diffusion would then be easy.

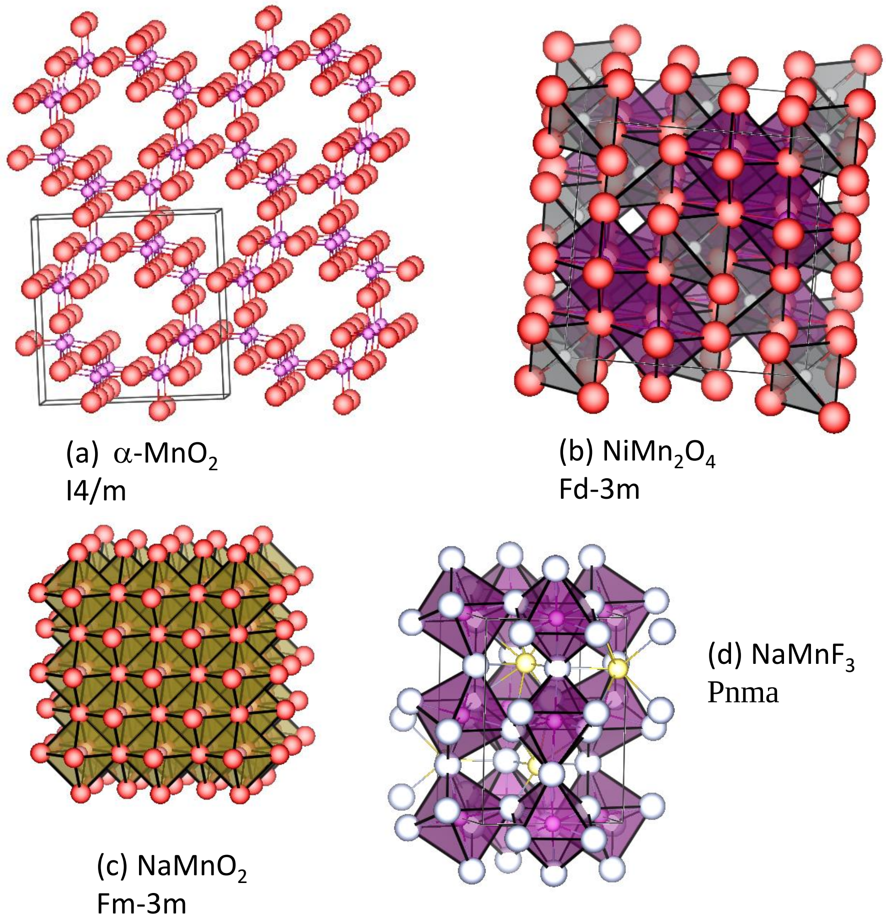

Figure 6. Structures of selected manganese compounds for sodium batteries. (**a**) Tetragonal α-MnO_2 (I4/m) [57]. (**b**) Cubic spinel $NiMn_2O_4$ [58]. (**c**) Cation-disordered rock salt-type $NaMnO_2$ [59]. (**d**) Perovskite-type $NaMnF_3$ [60].

Li et al. obtained nanoparticles of α-MnO_2 with feather-like morphology in situ grown on carbon paper via hydrothermal method [61]. This nanostructured electrode is binder-free. The composite material α-MnO_2/carbon paper may possess pseudocapacitive behavior, a working voltage between 0 and 3.0 V, and it delivers a maximum reversible capacity of 519 mAh g^{-1} and about. 300 mAh g^{-1} after 400 cycles.

Silver atoms can incorporate into the structure of α-MnO_2 [62], leading to silver hollandite ($Ag_xMn_8O_{16}$) isostructural to α-MnO_2 (PDF # 01−077−1987). Silver atoms are in the middle of the tunnels and are electrochemically active. During the discharge process and sodium intercalation into $Ag_{1.22}Mn_8O_{16}$, silver ions reduce to silver metal (cubic Ag) through a reduction-displacement reaction, the charge transfer resistance is decreased, and the crystallinity is reduced for $Na_8Ag_{1.22}Mn_8O_{16}$. The structure is unstable for a wide voltage window (3.8–1.3 V vs. Na^+/Na) and a high sodiation level.

The polymorph β-MnO_2 phase exhibits better electrochemical performance and cyclability than α-MnO_2 [63]. The tetragonal phase β-MnO_2 (JCPDS no. 24-0735) possesses a tunnel density of two tunnels per formula unit (0.104 $Å^{-2}$), which is more than twice that of α-MnO_2 [64]. According to the XRD results, the lattice of β-MnO_2 slightly expands during the reversible sodium intercalation, and a small amount of $NaMn_2O_4$ (s.g. Pnam) forms during the cycling process while the tetragonal phase β-Na_xMnO_2 is maintained as the main phase. The nanorods particles of β-MnO_2 deliver an initial capacity of 350 mAh g^{-1} in sodium cells, and the reversible capacity is about 200 mAh g^{-1} after 100 cycles. The formation of $NaMn_2O_4$ could be the main cause of the gradual capacity deterioration.

2.5. Amorphous MnO_2

Amorphous materials can be an alternative to well-crystallized structures for sodium intercalation. As a result of the amorphous character, the higher concentration of interfacial regions and the small particle size could facilitate rapid sodium diffusion and excellent cyclability. Spherical particles of mostly amorphous MnO_2 with a 20–60 nm diameter can be prepared by reduction of $KMnO_4$ in ethanol [65]. The capacity was maintained at about 137 mAh g^{-1} after 100 cycles, with just a 5% decay of the initial capacity. The charge transfer at the electrode–electrolyte interface improved during the electrochemical cycling of amorphous manganese dioxide. However, a disadvantage is the intrinsic low electronic conductivity at room temperature of MnO_2, which limits the rate capability.

2.6. Spinel-Type $NaNi_{0.5}Mn_{1.5}O_4$

The insertion of sodium into the spinel structure proceeds at a significantly lower voltage than for lithium (typically ca. 1 V lesser). To compensate for that, the redox pair Ni^{4+}/Ni^{2+} can increase the average cell voltage of the spinel electrode by about 0.6 V compared to Mn^{4+}/Mn^{3+} [10,66]. Sodium intercalation in $Ni_{0.5}Mn_{1.5}O_4$, which is prepared by the delithiation of $LiNi_{0.5}Mn_{1.5}O_4$, occurs exclusively at 8a tetrahedral sites at ca. 3.6 V. Spinel-type $NaNi_{0.5}Mn_{1.5}O_4$ exhibits poorer electrochemical performance in sodium cell than $LiNi_{0.5}Mn_{1.5}O_4$ in lithium cell. The main reason for that can be the larger size of Na^+ than Li^+ and the structure distortion induced by the desodiation [67]. The lattice mismatch between sodiated and desodiated spinel results in larger stresses and low cyclability.

Kim et al. theoretically studied the replacement of Mn by Ti in the spinel $Na_{1-x}[Ni_{0.5}Mn_{1.375}Ti_{0.125}]O_4$ by DFT calculations [68]. The lower electronegativity of Ti could increase the ionicity of the bonding and then help stabilize the crystal structure. The bond Ti-O is stronger than the bond Mn-O. In addition, the larger ionic radii of Ti^{4+} in octahedral coordination (TiO_6) would widen the diffusion path of Na^+. The amount of Ti must be limited to avoid the formation of many Jahn–Teller ions Mn^{3+}. Nickel would be the only redox center (Ni^{4+}/Ni^{2+}) during the electrochemical cycling. Ti-doping theoretically mitigates phase segregation, stabilizes the intermediate state, and improves reversibility and cyclability. The positive effect of Ti-doping in $LiNi_{0.5}Ti_xMn_{1.5-x}O_4$ was experimentally checked in lithium cells [69], but it seems that $Na_{1-x}[Ni_{0.5}Mn_{1.375}Ti_{0.125}]O_4$ in sodium cells has not yet been experimentally studied.

2.7. Disordered Rock Salt Oxide

Stochiometric $NaMnO_2$ with a cation-disordered rock salt-type structure is a metastable polymorph of sodium manganate in which sodium and manganese atoms occur evenly distributed in the same crystallographic site (Figure 6). The reversible capacity (200 mAh g^{-1}) in Na cell is higher, the oxidation from Mn^{3+} to Mn^{4+} is highly reversible, and the capacity retention is much better for the nanocrystalline sample obtained by mechanical milling [70]. Na_3NbO_4 is non-conductive and electrochemically inactive. The mechanical milling of a mixture of Na_3NbO_4 and $NaMnO_2$ creates a cationic-disordered rock salt structure in which the Mn^{3+} ions promote electronic transport [70]. The theoretical capacity of $Na_{1.3}Nb_{0.3}Mn_{0.4}O_2$ is 311 $mAhg^{-1}$, but the maximum experimental capacity is 200 mAh g^{-1} at 50 °C. During the first charge and extraction of 0.4 Na per formula, Mn oxidizes to Mn^{4+}, but during the discharge, manganese reduces to Mn^{2+}. Crystallinity diminishes upon electrochemical cycling, and oxygen may evolve during charging. However, niobium is expensive, so Earth-abundant elements such as titanium should replace it. Much better capacity retention was achieved for Nb-free $Na_{1.14}Mn_{0.57}Ti_{0.29}O_2$, and this capacity was ascribed to Mn^{3+}/Mn^{4+} and anionic O^{2-}/O^{n-} redox [71].

2.8. Spinel-Type $Li_4Mn_5O_{12}$

The cubic spinel $Li_4Mn_5O_{12}$ allocates three Li in tetrahedral sites and one in octahedral sites, and it is unstable and decomposes to Li_2MnO_3 and $LiMn_2O_4$ at temperatures above 600 °C [72]. Zhang et al. reported that $Li_4Mn_5O_{12}$ can reversibly accommodate sodium through a voltage plateau at ca. 2.9 V vs. Na^+/Na, and with a maximum capacity of ca. 140 mAh g^{-1} (corresponding to 2.2 Na per formula unit) [73]. The capacity is higher for the sample obtained at a lower temperature (400 °C). During charging, Li ions are also removed from the spinel, and $Na_xLi_{4-y}Mn_5O_{12}$ is formed. The structural changes caused by the sodium-lithium exchange, and the loss of crystallinity upon cycling, originate poorer cycling performance.

2.9. Birnessites

Sodium birnessite, $Na_xMnO_2{\cdot}yH_2O$, contains crystal water in its layered structure, which may help to reversibly form a metastable spinel-like phase [74]. In contrast to other unwanted and irreversible layered/spinel transformations during alkali ion (de)intercalation, the birnessite can sustain the transformation between the phases. The energy barrier for the migration of the Mn ion from octahedron in the Mn layer to tetrahedron in the Na layer can decrease with the crystal water. Interestingly, the structural water of the birnessite can also be a way to provide high mobility of Mg^{2+} in the oxide framework [75]. The presence of lattice water is strongly associated with sodium storage performance, which is ascribed to the stabilization of the layered structure and the improvement of sodium diffusivity during cycling [76]. Varying the end-of-charge voltage can control the amount of water in the interlayer space. When charged at high voltage, the network water can be withdrawn from the layered structure, simultaneously contributing to a larger reversible capacity and high coulomb efficiency [77].

2.10. $MgMn_2O_4$ and $Mg_xMn_{2-y}Fe_yO_4$

Small guests, such as Li^+ and Mg^{2+}, tend to prefer tetrahedral sites in oxide spinel hosts, while larger Na^+ ions prefer octahedral sites [14,78]. Cation diffusion in the spinel occurs through successive hops between octahedral and tetrahedral sites, and this fact constrains sodium diffusion. $MgMn_2O_4$ is susceptible to site inversion.

As a new strategy, it has been proposed to firstly remove some magnesium ions from the tetragonal spinel $MgMn_2O_4$, and later to intercalate sodium. [15], for example by oxidation in an electrochemical cell and by chemical disproportionation. The capacity for sodium intercalation in the sample that was not treated with acid is low (31 mAh g^{-1}). However, Mg ions can be deintercalated from $MgMn_2O_4$ by disproportionation of Mn(III) in acid solution and dissolution of Mn(III) ions [15], and the resulting compound, $Mg_xMn_2O_4$ ($x < 1.0$), possesses cationic vacancies that can increase the capacity for sodium intercalation. Sodium reversibly intercalates into $Mg_{0.03}Mn_2O_4$, delivering a capacity of ca. 100 mAh g^{-1} in the voltage range between 4.1 and 1.9 V. Limiting the charge capacity (or upper cut-off voltage) was critical to achieving good electrochemical cycling, which is in good agreement with the results of Yabuuchi et al. [11].

Medina et al. explored $MgMn_{2-y}Fe_yO_4$ as an electrode for sodium-ion batteries [15]. They proposed that magnesium can help stabilize the structure of the spinel during sodium intercalation, while iron can decrease the irreversible decomposition of the electrolyte solution. The partial replacement of Mn by Fe can decrease the electrolyte decomposition catalyzed by Mn^{4+} on the electrode surface. However, they still only achieved acceptable capacity retention when the upper cut-off voltage was below 4.4 V (Figure 7).

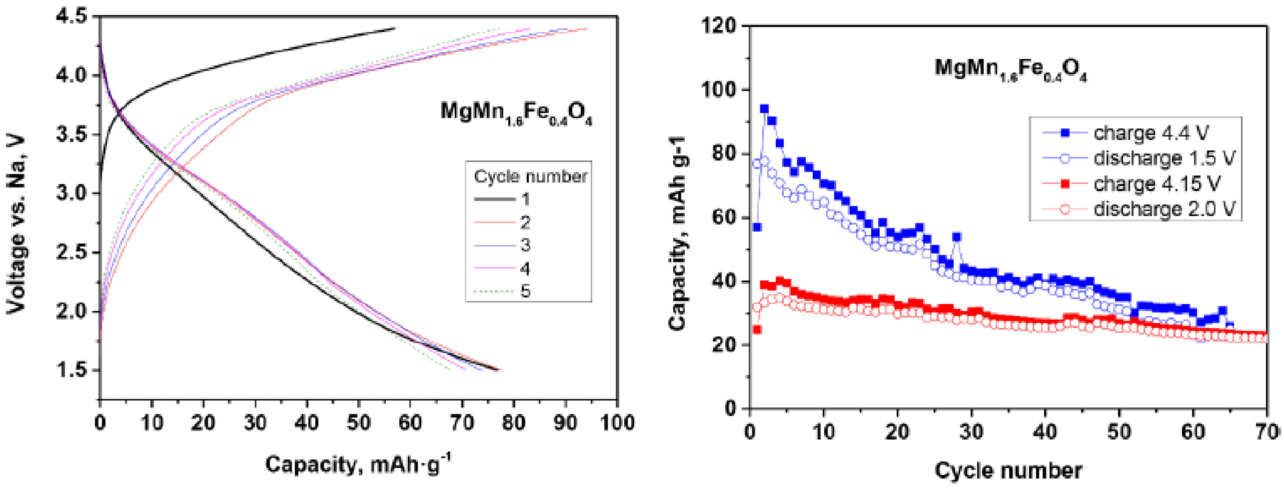

Figure 7. Electrochemical properties of spinel-type $MgMn_{1.6}Fe_{0.4}O_4$ in sodium cell. Reprinted (adapted) with permission from Ref. [15]. License Number 5560700952879 (Elsevier).

3. Sodium Manganese Fluorides and Oxyfluorides

$NaM_{1-x}Mn_xF_3$ series with M = Fe, Mn, and Co crystallizes in the orthorhombic space group Pnma with a perovskite-type structure [79] (Figure 6). Although the perovskites generally offer many possibilities for different applications, the atomistic simulations suggest that the energy barrier for sodium diffusion through a three-dimensional path is relatively high in $NaM_{1-x}Mn_xF_3$.

Nava-Avendaño et al. studied the fluoro-perovskites Na_2MnF_5 (s.g. $P2_1/c$), $NaMnF_3$ (s.g. Pnma), and unidentified phase of metastable sodium manganese oxyfluoride [80], but the electrochemical (de)insertion of Na in these materials was not practically reached. The strong oxidative decomposition of the electrolyte solution by this fluoride was pointed out. Later, Kitajou et al. reported that the perovskite-type $NaMnF_3$, after ball-milling with 20 wt.% of acetylene black, is promising as electrodes for sodium-ion batteries [81]. The theoretically calculated voltage for Na_xMnF_3 ($0 < x < 1.0$) is ca. 4.0 V. The $NaMnF_3$/carbon composite mixture has an initial reversible capacity of 89 mAh g^{-1} in the voltage range between 2.0 and 4.3 V, and only 40 mAh g^{-1} after 20 cycles. Thus, it seems that the manganese fluoride can operate at very high voltages, but the capacity retention is not good, most likely due to the decomposition of the electrolyte solution. The theoretical calculations indicated that $NaMnF_3$ has three voltage plateaus for the ranges of $0 < x < 0.5$ (3.84 V), $0.5 < x < 0.75$ (3.9 V), and $0.75 < x < 1$ (4.55 V). and the experimental voltage agrees well with the DFT calculations [81].

The sodium insertion into the F-doped spinel $Li_{1.1}Mn_{1.5}Ni_{0.5}O_{3.8}F_{0.2}$ was studied by Kim and Amatucci [66]. For that purpose, firstly Li was electrochemically removed from $Li_{1.1}Mn_{1.5}Ni_{0.5}O_{3.8}F_{0.2}$, and λ-$Mn_{1.5}Ni_{0.5}O_{3.8}F_{0.2}$ was obtained. The lower voltage of sodium intercalation compared to lithium intercalation (ca. 1.0 V lower) could be partially compensated by the inductive effect of fluorine. The full sodiation of the spinel was achieved, but it was found that the kinetics of the sodium insertion was very limited by the particle size of the spinel.

The oxyfluoride with nominal composition Na_2MnO_2F has a disordered rock salt structure where Na and Mn randomly occupy 4a octahedral sites, and O and F occupy 4b sites [82]. The initially observed reversible capacity of ca. 220 mAh g^{-1} at a slow rate corresponds to the desodiation of 1.7 Na per formula and the Mn^{3+}/Mn^{4+} redox pair. The capacity is stable during 50 cycles (100 mAh g^{-1} at a high rate). The possible reasons for the observed capacity after further cycles loss can be irreversible anionic redox of oxygen and manganese dissolution.

Anionic doping can strongly modify the crystallographic structure of sodium manganese oxide. Zan et al. reported that after F-doping the tunnel-type $Na_{0.4}MnO_2$, the resulting compounds with general $Na_xMnO_{2-y}F_y$ can be described as an intergrowth of tunnel-type and layer-type (P2) structures, and it exhibits improved cycling stability [83]. As the fluorine content increases, the layer/tunnel ratio increases. The substitution of Mn by Al and O by F in tunnel-type $Na_{0.4}MnO_2$ results in a P2-type layered structure (s.s. P63/mmc) for the compound $Na_{0.46}Mn_{0.93}Al_{0.07}O_{1.79}F_{0.21}$ [84]. For $Na_{0.66}[Mn_{0.66}Ti_{0.34}]O_{2-x}F_x$ ($x < 0.1$) with tunnel-type structure, the lattice cell parameters can be tuned by controlling the F-doping [85]. The F-doping enlarges the size of the S-shape tunnels, and this can be related to the electronegativity of fluorine. In addition, F-doping prevents the unit cell change during (de)sodiation and cycling is improved (1000 cycles).

4. Polyanion Compounds

As compared with oxides, polyanion-type active cathode materials offer important advantages in Na-ion batteries. First, the framework of anions, e.g., the structures shown in Figure 8, is commonly very stable and hinder electrode degradation upon cycling. Second, the larger interstices in the structure permit the transport of relatively large sodium ions through the structure. Finally, the strong covalent oxygen bonds with the central atom of the oxoanions impede oxygen evolution, with the subsequent improvement in safety. On the contrary, the electronic conductivity is limited by the anions blocking the contact between the orbitals of the transition metal ions. In addition, the larger molecular weight of the polyanion as compared with an oxide anion may reduce the overall specific capacity. Nevertheless, successful polyanionic materials are nowadays one of the most used cathodes in LIBs.

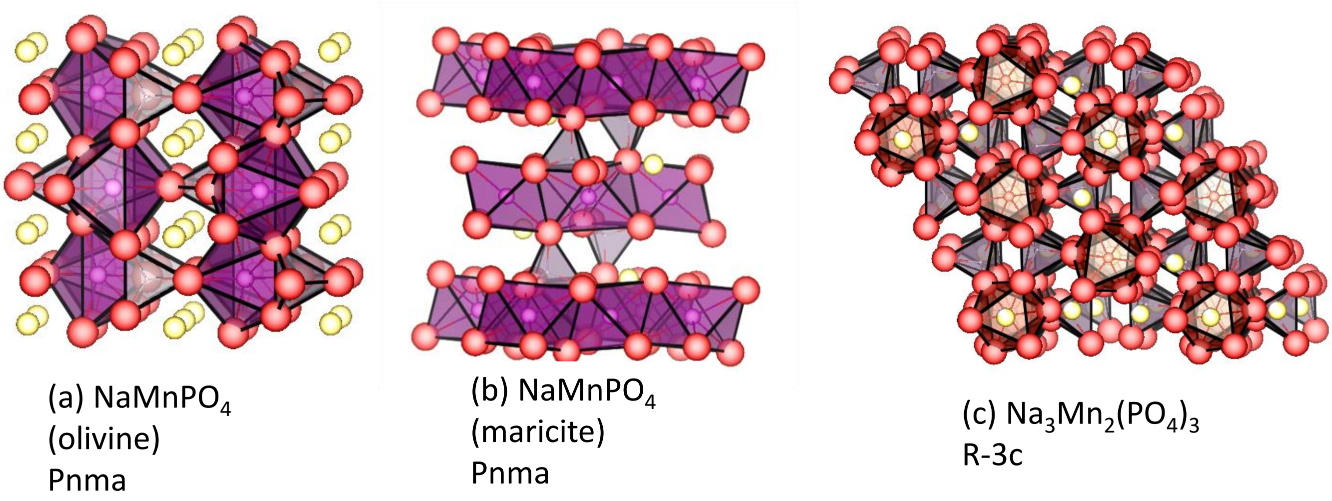

Figure 8. Structures of selected manganese compounds for sodium batteries based on polyanions. (**a**) Maricite-type $NaMnPO_4$. (**b**) Olivine-type $NaMnPO_4$. (**c**) NASICON-type $Na_3Mn_2(PO_4)_3$.

4.1. Maricite and Olivine

An analogous composition to the successful olivine-structure $LiFePO_4$ in LIBs is known for sodium and manganese. $NaMnPO_4$ crystallizes in two closely related but different structures: olivine (o-NMP) type and maricite (m-NMP) (Figure 8). The framework of both modifications is composed of the phosphate groups, while the metals occupy two sets of equivalent positions commonly referred to as M1 and M2. The structural difference results from the occupancy of these sites: Na^+ in M1 and Mn^{2+} in M2 for the olivine structure, while the opposite is true for the maricite structure [86]. In the olivine structure, sodium octahedra order in such a way that form zig–zag chains along the b-axis, which ensure a favorable intercalation pathway for alkali ions [87]. Contrary to the olivine structure, the reverse cationic distribution in the maricite structure blocks the pathways for Na^+ diffusion, thus the maricite is electrochemically inactive [88]. However, the experimental findings demonstrate that the electrochemical performance of m-NMP is boosted by choosing an appropriate synthesis procedure. In this way, Venkatachalam et al. reported the preparation of well-crystallized and pure maricite $NaMnPO_4$ nanorods by a polyol procedure [89]. This material displayed interesting electrochemical activity in sodium half-cells, with an initial specific discharge capacity of 102 mAh g^{-1} at 0.1 C [89]. Based on first-principles calculations, it has been demonstrated that the maricite $NaMnPO_4$ becomes a semiconductor upon sodium extraction, which occurs in a voltage window between 5.132 V and 4.655 V [90].

Regarding o-NMP, its electrochemical activity was improved by a different approach. Thus, Boyadzhieva et al. [91] used an Mg-doping strategy, which strongly modified the olivine structure by incorporating the doping Mg^{2+} anions in the Na^+ sites. As a result, reversible capacities close to 100 mAh g^{-1} resulted for sodium half-cells in the 2.1–4.5 V interval. Calculations predict that the doping of o-NMP with Sb causes an enhancement in electronic conductivity and Na diffusion, which is of importance in improving the electrochemical performance of o-NMP [92]. The doping approach seems more effective in respect of the storage properties of o-NMP than the classical approach including the carbon coating of o-NMP [91].

4.2. Fluorophosphates

In contrast with the layered structure of Na_2FePO_4F, the manganese compound Na_2MnPO_4F occurs as a 3D tunnel monoclinic structure belonging to the P21/n space group [93]. Wu et al. first reported a significant capacity (98 mAh g^{-1}) in sodium cells [94]. In addition, they prepared different mixed salts in the $Na_2Fe_{1-x}Mn_xPO_4F$ and found that for x = 0.3 or higher, the structural transition from 2D to 3D took place. For x = 0.5, Xie et al. reported a capacity of 107 mAh g^{-1} in the 2.0–4.5 V interval [95]. The electrochemical activity of Na_2MnPO_4F was boosted by decreasing particle size and carbon coating, which led to an initial discharge capacity of 98 mAh g^{-1}. More recently, a specific capacity of 120 mAh g^{-1} was reported for Na_2MnPO_4F obtained by a sol-gel route with a citric acid precursor of the carbon coating. The observed cell potential was between the values obtained by first-principles calculations for the following reactions [96]:

$$Na_2MnPO_4F = NaMnPO_4F + Na \qquad 3.7\ V \tag{1}$$

$$NaMnPO_4F = MnPO_4F + Na \qquad 4.7\ V \tag{2}$$

4.3. Carbonophosphates

In general, sodium manganese phosphates display worse electrochemical performance than sodium iron phosphates. To take advantage of manganese-based polyanionic compounds over iron analogues, sodium manganese carbonophosphates emerge as a new family of electrodes for SIB. The first member of this family is sidorenkite—$Na_3MnPO_4CO_3$ [97–99]. The structure consists of double layers built from MnO_6 octahedra and PO_4 tetrahedra (Figure 9). The CO_3 groups are located between double layers to ensure two different crystal positions for Na atoms. From the structure of $Na_3MnPO_4CO_3$, two Na per formula unit can be extracted thanks to the electrochemical activity of Mn^{2+}/Mn^{3+} and Mn^{3+}/Mn^{4+} redox couples, with the theoretical capacity being 191 mAh g^{-1}. Because of the low electronic conductivity, the electrochemical performance of carbonophosphates depends critically on the method of synthesis and electrode fabrication. Using the hydrothermal method followed by high-energy ball milling with carbon additives, Wang et al. succeeded in the preparation of nano-sized $Na_3MnCO_3PO_4$, which displays the enhanced electronic conductivity and specific capacity reaching 92.5% of its theoretical one [100,101].

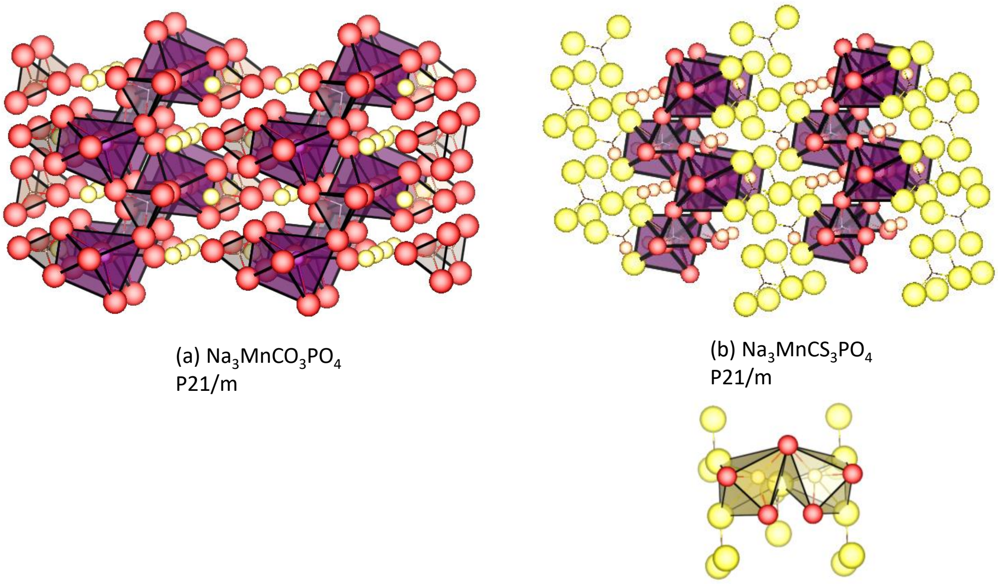

(a) $Na_3MnCO_3PO_4$
P21/m

(b) $Na_3MnCS_3PO_4$
P21/m

Figure 9. Structures of (**a**) $Na_3MnPO_4CO_3$ and (**b**) $Na_3MnPO_4CS_3$ [102].

According to new DFT calculations on carbonophosphates, the replacement of O by S expands the lattice, and the calculated voltage for sodium extraction from $Na_3MnPO_4CS_3$ is lower as compared to $Na_3MnPO_4CO_3$ [102]. Both oxygen (harder base) and sulphur (softer base) atoms surround each sodium atom in a distorted polyhedron (Figure 9). This type of coordination of a metallic element (Mn) surrounded by distinct types of anions (PO_4^{3-}, CO_3^{2-}, and CS_3^{2-}) resembles an energized or entatic state. In the entatic state of the metalloproteins, the protein that surrounds the metal ion imposes a distorted geometry to the coordination sphere of the metal-ligand complex, increasing the energy state of the metal and decreasing the activation energy for certain reactions. The coordination sphere which forms with ligands of different natures can increase the energy of the electrode material and decrease the activation energy for the charge/discharge process (Figure 10). The concept of an entatic state is so attractive that it extends to enzymes, organic chemistry, catalysis, metallorganic frameworks, and even electrode materials [102]. For example, the distortion of the unit cell due to the Jahn–Teller effect of Mn(III) in the spinels can be cancelled by this multianion approach [102], and the charge/discharge process may be more efficient.

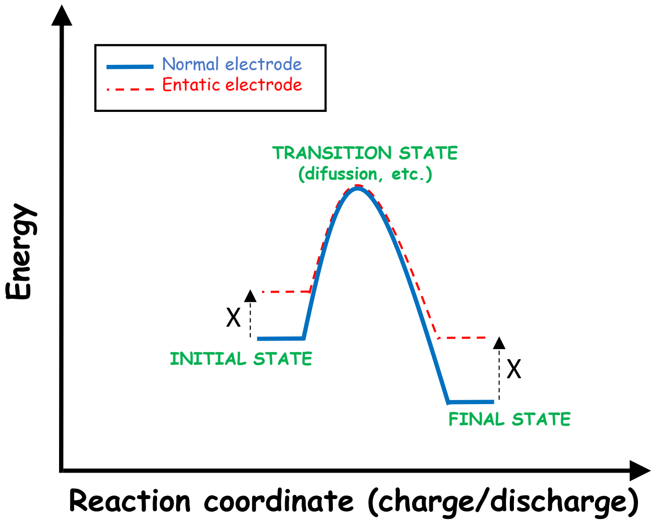

Figure 10. Schematic diagram for a one-step process of two types of electrode materials [102]. Continue blue line: normal process. Dotted red line: entatic state path. The strain energy is X.

4.4. NASICON-Related Compounds

A thoroughly studied polyanionic cathode material is $Na_3V_2(PO_4)_3$ (NVP) with a NASICON-related structure (Figure 8). It generates from "lantern" units of three PO_4 tetrahedra sharing corners with two VO_6 octahedra. These units link to others defining different sets of equivalent positions available to sodium. The resulting material has high ionic conductivity but poor electronic conductivity, thus needing composites with conductive carbon. NVP in sodium half-cells displays electrochemical activity in a wide range of working potentials (0.3–4.7 V) with different plateaus. The most common cathodic activity involves a 3.6 V plateau in which two Na can be reversibly extracted from the initial NVP stoichiometry. A second plateau around 4.6 V could extract the third sodium.

The most common preparative route reported for the NASICON phosphates is the citric-based sol-gel method. This procedure generates a reducing atmosphere during the calcination step in inert atmosphere. It allows both to preserve a low valence state in the transition metals and coat the active material with a conductive carbon phase. Notwithstanding, alternative synthetic procedures have allowed researchers to design new morphologies [103], 3D pore structures [104], and new carbon composites [105] to optimize their electrochemical behavior. The replacement of vanadium by manganese could provide extra value to this system because of its greater abundance and being more environmentally friendly. First-principles calculations on $Na_xMn_2(PO_4)_3$ revealed low favorable formation energies [106]. The possible participation of different redox pairs Mn^{3+}/Mn^{2+} and Mn^{4+}/Mn^{3+} was also shown. However, the Jahn–Teller distortion of the Mn^{3+} ions impedes its use as the only transition metal in the structure. For these reasons, manganese usually appears combined with other metals. Zhou reported $Na_4MnV(PO_4)_3$ in which Mn^{3+}/Mn^{2+} and V^{4+}/V^{3+} redox couples are respectively accessed at 3.6 and 3.3 V, delivering an initial efficiency as high as 97% and long cycling durability at 10 C [107]. This compound can be prepared in a fibrous particle morphology by using a surfactant-assisted method. According to XPS data, the presence of V^{3+}, Mn^{2+}, and Mn^{3+} accounted for the sodium-rich stoichiometry. The material displayed an interesting specific capacity of 58 mAh g^{-1} when cycled at 5 A g^{-1} and a capacity retention of 85.1% over 1200 cycles at 1 A g^{-1} [108]. In addition, two pairs of apparent plateaus at around 3.4 V and 3.6 V vs. Na^+/Na are ascribed to the V^{3+}/V^{4+} and Mn^{2+}/Mn^{3+} redox pairs, respectively.

Zirconium was also combined in 1:1 proportion with manganese in $Na_3MnZr(PO_4)_3$ and the nanometric particles prepared by Gao et al. [109]. The authors suggested that although the $Mn^{3+}O_6$ octahedra are distorted on the local scale, the cooperative Jahn–Teller distortion that would result in a long-range ordering of the Na ions is suppressed in this cathode material. In consequence, the material exhibited excellent cycling stability and 91% capacity retention after 500 cycles at 0.5 C rate. $Na_3MnZr(PO_4)_3$ co-functionalized with semi-graphitic carbon and reduced graphene oxide was evaluated by Zhu et al. [110]. When used as the cathode in sodium half cells, it provided a reversible capacity of 114 mAh g^{-1} at 0.2 C. The dual carbon functionalized material was also evaluated in full SIB vs. soft carbon, which delivered an initial discharge capacity of 97 mAh g^{-1} and 73% after 100 cycles at 0.2 C. However, the initial coulombic efficiency was low but increased upon cycling. More recently, Ma et al. achieved excellent performance at 50 C and long-term cycling stability in a wide temperature range by preparing a composite of reduced graphene oxide and amorphous carbon in $Na_3MnZr(PO_4)_3$ microspheres. The resulting interconnected conductive network provided high porosity and specific surface area, allowing to accommodate the volume changes, and achieving fast sodium storage by ameliorating the electrode–electrolyte interface [111].

The combination of manganese with titanium in $Na_3MnTi(PO_4)_3$ has also attracted more attention due to the eco-friendly and low-cost benefits of these elements. Gao et al. first reported this composition as a structurally stable framework able to deliver two sodium ions per formula unit through access to both Mn^{3+}/Mn^{2+} and Mn^{4+}/Mn^{3+} redox couples (Figure 11). The minimum voltage gap of 0.5 V between these plateaus favors the applicability of this electrode material as a high-voltage cathode for sodium-ion batteries [112,113]. Further reports have even remarked the possibility of assembling symmetric full cells with $Na_3MnTi(PO_4)_3$ as both positive and negative because of the significant differences in the potential of the distinct redox couples of $Mn^{3+/4+}$ (ca. 4 V) and $Ti^{3+/4+}$ (ca. 2 V) [113]. Notwithstanding, its poor electronic conductivity requires carbon coating to achieve adequate rates of electron transfer. Different authors have proposed interesting strategies to prepare highly conductive carbon composites. Thus, Li et al. reported graphene-encapsulated $Na_3MnTi(PO_4)_3$ particles with carbon-shell covering material. The synergistic effect of this multifunctional 3D conductive network enhances the contribution of pseudocapacitance to eventually provide outstanding rate capability and cycling stability [114]. Otherwise, $Na_3MnTi(PO_4)_3$ particles embedded in a nitrogen-doped carbon matrix are evidenced to be an interesting solution to enhance the electronic conduction of this NASICON material, resulting in a notorious improvement of the specific capacity and high-rate capability [115].

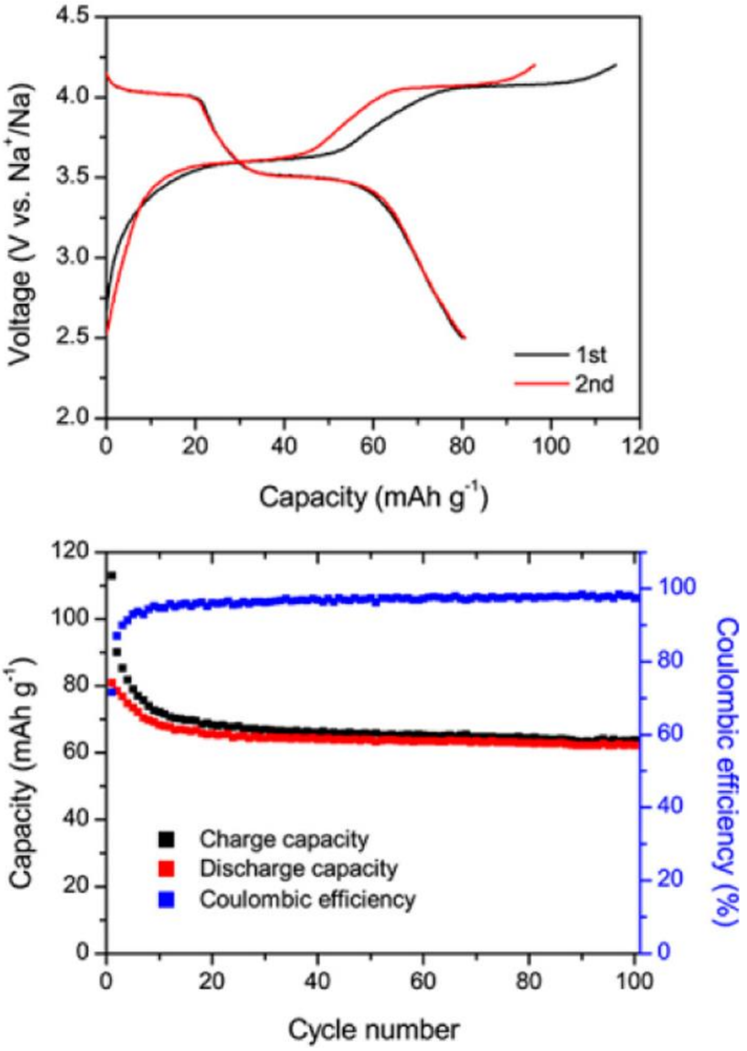

Figure 11. Electrochemical properties of NASICON-type $Na_3MnTi(PO_4)_3$ in sodium cell. Reprinted (adapted) with permission from Ref. [112]. Copyright (2016) ACS.

The incorporation of chromium in $Na_4MnCr(PO_4)_3$ has also been proposed as an interesting three-electron reaction, involving Mn^{2+}/Mn^{3+}, Mn^{3+}/Mn^{4+}, and Cr^{3+}/Cr^{4+} redox couples, which can deliver a high energy density (566.5 W h kg^{-1}) for this kind of phosphate Na-storage cathode material [116]. Alternatively, the partial replacement of manganese and vanadium by this transition metal has led to a significant improvement in sodium diffusivity along with a net gain of the reversible extraction of sodium at either low or high rates [117,118]. Eventually, Zheng et al. synthesized the aluminum-containing compound by a sol-gel method. Despite the economic and environmental benefits and higher energy density as compared to vanadium compound, $Na_3MnAl(PO_4)_3$ exhibited low capacity and undesirable cycling stability [119].

4.5. Silicates

As in the case of carbonophosphates, sodium manganese silicates can intercalate Na^+ ions through a two-electron reaction due to the redox couples $Mn^{2+}/Mn^{3+}/Mn^{4+}$ [120]. This allows us to achieve extremely high capacities. The structure of polyanionic $Na_2MnS_iO_4$ is depicted in Figure 12. The monoclinic Na_2MnSiO_4 covered with an amorphous carbon film with a thickness of around 2–3 nm delivers the highest specific capacity (i.e., 210 mAh g^{-1}) in comparison with other polyanionic compounds [121]. The excellent electrochemical properties of Na_2MnSiO_4 are a result of the energetically favorable diffusion of Na^+, which is faster than Li^+ diffusion into Li_2MnSiO_4 [122]. The Na ion diffusion takes place by 3D path with the migration energy of 0.81 eV [123]. Further improvement of the electrochemical properties of Na_2MnSiO_4 through selective doping with aliovalent Al^{3+} ions needs to be proven experimentally [123].

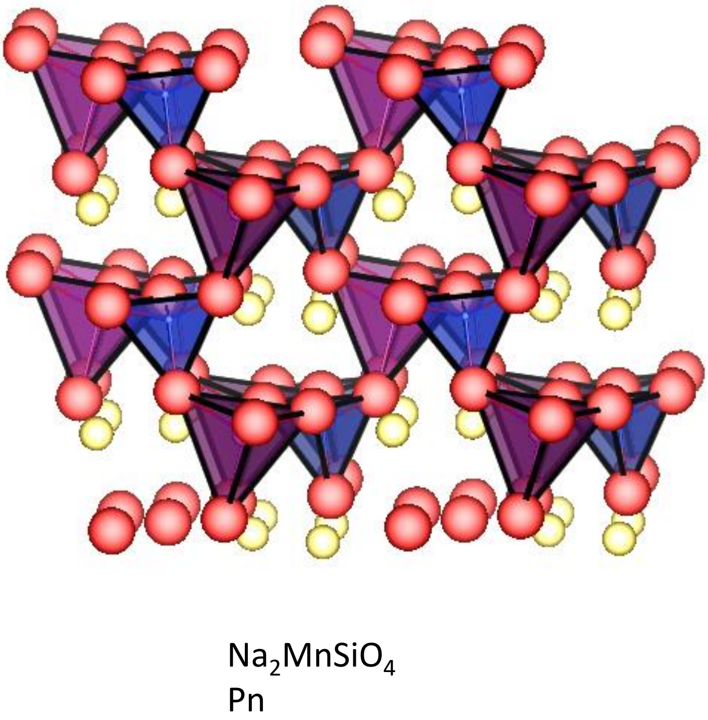

Figure 12. Structure of Na_2MnSiO_4.

5. Prussian Blue Analogues

Goodenough's group pointed out that the bond between oxygen and sodium can impede its motion while the replacement of O^{2-} by CN^- decreases the activation energy for sodium transfer and, thus, sodium manganese hexacyanoferrate is attractive as a cathode [124]. Metal hexacyanoferrates with general formula $A_xM[Fe(CN)_6]_y \cdot zH_2O$, where A = Li, Na, K, etc., M = Fe, Mn, Co, Ni, Cu, etc., $0 < x < 2$, and $0 < y < 1$, are known as Prussian Blue analogues (PBAs) [125]. Sodium ions easily accommodate in the spacious channels of the PBAs, which typically possess a face-centered cubic unit cell (s.g. Fm-3m). This structure provides rapid sodium mobility. The crystal structure of sodium manganese hexacyanomanganate ($Na_xMn[Mn(CN)_6]$) depends on the sodium content and oxidation state of manganese. $Na_2Mn^{II}[Mn^{II}(CN)_6] \cdot 2H_2O$ possesses a monoclinic structure (s.g. P21/n), which is atypical for PBAs (Figure 13) [126]. After oxidation of all the Mn to

Mn(III), the structure of $Mn^{II}[Mn^{II}(CN)_6]$ is the typical cubic perovskite (Fm-3m), while the structure of the fully reduced electrode ($Na_3Mn^{II}[Mn^{I}(CN)_6]$) is monoclinic ($P2_1$). The capacity $Na_2Mn[Mn(CN)_6$ is very high (209 mAh g^{-1} at 40 mA g^{-1}) [127]. Hurlbutt et al. found by DFT that $Na_3Mn^{II}[Mn^{I}(CN)_6]$ and the hydrated form $Na_3Mn^{II}[Mn^{I}(CN)_6]\cdot 2H_2O$ are thermodynamically stable, despite including the rare Mn(I) [128].

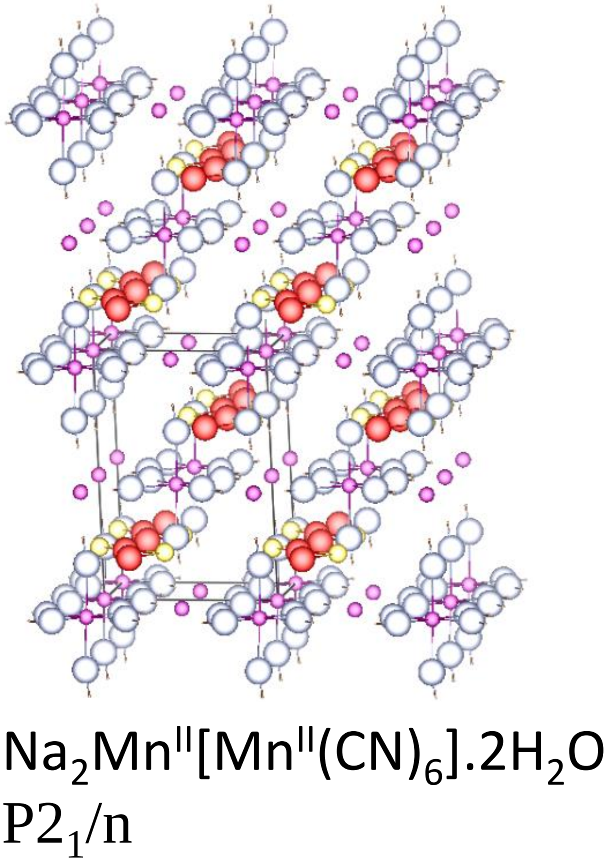

Figure 13. Structure of $Na_2Mn^{II}[Mn^{II}(CN)_6]\cdot 2H_2O$ [126].

It seems that the vacancies of $Fe(CN)_6$, the water molecules, and the structure disturbances caused by the redox reactions can deteriorate the life cycle of PBAs. To improve the cycling stability, it has been proposed to employ $Na_2Ni_xMn_yFe(CN)_6$, where nickel is electrochemically inactive [129]. The compositional disorder would affect the electrochemical reaction. Using a high-entropy material, the phase transition and structural degradation could be suppressed [130]. The DFT calculations unveiled that the structure of the high-entropy PAB is more robust, and the partial replacement of Mn by Ni could contribute to this disorder. Creating a Ce-rich shell on the PBAs particles could improve the stability of the electrode–electrolyte interface [131]. A copper-containing coating layer obtained by a simple exchange method is another option [132].

6. Conversion-Type Electrodes

As early as 2000, Jean Marie Tarascon group first reported the use of binary transition metal oxides as anode material for lithium-ion batteries [133]. In this concept, metal reduction to the metallic state together with the formation of lithium oxide were found to occur together with particle comminution and pseudocapacitive phenomena on the deep discharge of lithium test batteries. The process was partially reversible with the regeneration of transition metal oxides with a highly dispersed nature upon cell charge. Poizot et al. also anticipated the difficulties in reducing MnO to Mn metal by Li [134].

The conversion anode concept was further extended to mixed transition metal oxides [135–139] and oxalates [140–142]. For example, low-cost Ni_6MnO_8 (s.g. Fm3m) material was proposed as anode for lithium-ion batteries in 2002, with an experimental reversible capacity of ca. 700 mAh g^{-1}, and the proposed discharge-charge mechanism involved the following reactions [136,143]:

$$Ni_6MnO_8 + (12 + x)\ Li = 6Ni + 6Li_2O + Li_xMnO_2 \tag{3}$$

$$NiO + 2Li = Ni + Li_2O \tag{4}$$

Later studies found that metallic Mn can be formed when MnO_x oxides are discharged down to 0.0 V vs. Li^+/Li [144,145]. Another conversion electrode material based on Mn oxide for lithium batteries reported in 2002 was $MnCo_2O_4$, but it exhibits high irreversibility and low coulombic efficiency in the first cycle [146].

In 2002, we also reported the first conversion electrodes to the anode of sodium-ion batteries, using the spinel $NiCo_2O_4$ in the form of nanoparticles obtained by the calcination of oxalates. A full Na-ion cell was also studied, using Na_xCoO_2 as the cathode material [137]. This possibility was developed in further work by extending the concept to other oxides and oxysalts [147–149]. The general equation to describe the conversion process in oxides is:

$$MO_x + 2xe^- + 2xNa^+ \rightarrow M + xNa_2O \tag{5}$$

where M represents single or multiple transition metals with an average oxidation state of +2x. In addition to this conversion-type reaction, it is generally accepted that the pseudocapacitive behavior also contributes to the capacity of these electrodes. A main drawback is that the volume change of the electrode material during the charge-discharge is even larger for sodium than lithium.

Although it is generally accepted that Fe, Co, Ni, Cu, and Nb oxides are particularly attractive as potential conversion anodes in Na-ion batteries [150], recent reports have examined the possible extension to manganese oxides. This section is focused on the electrodes based on manganese compounds, which would be used as conversion anodes in sodium-ion batteries and involve reduction down to ca. 0 V vs. Na^+/Na.

6.1. Manganese Oxides

To achieve good electrochemical performance, the particles of MnO are prepared with special morphologies and in the form of MnO-carbon composites. Cauliflower-like MnO-carbon composite materials prepared by a hydrothermal method have been studied in both sodium and lithium half-cells. Although the capacities and capacity retention were superior in lithium cells, the material displayed 123 mAh g^{-1} with good retention up to 200 cycles [151]. The composite formed by ultrasmall MnO nanoparticles (ca. 4 nm of diameter) supported on N-doped carbon nanotubes displays exceptional rate capability (709 mAh g^{-1} at 0.1 A g^{-1}) and ultralong cycling life (273 mAh g^{-1} after 3000 cycles) [152]. During the initial discharge, manganese oxide particles anchored on carbon nanotubes are reduced through a conversion reaction:

$$MnO + 2Na^+ + 2e^- \rightarrow Mn + Na_2O \tag{6}$$

During the subsequent charge, manganese is reversibly oxidized:

$$Mn + Na_2O \rightarrow MnO + 2Na^+ + 2e^- \tag{7}$$

The carbon nanotubes enhance the electronic conductivity and improve the stability of the electrode.

Sun et al. have questioned the use of MnO as a conversion electrode for SIB because the thermodynamic driving force for sodium storage is lower compared to lithium [153], and the change of the Gibbs energy for conversion reaction (6) is $\Delta G = -13.5$ kJ mol^{-1}, while for lithium it is more exergonic:

$$2Li + MnO = Li_2O + Mn,\ \Delta G = -198.3\ \text{kJ mol}^{-1} \tag{8}$$

Jiang et al. [154] studied different transition metal oxides as potential conversion-type anodes for SIBs. Among them, Mn_3O_4 thin films were found to deliver a first discharge capacity of 257 mAhg^{-1} and retained 61% of the initial charge capacity after 200 cycles. The electrochemical performance of Mn_3O_4 was found to be better than those of Co_3O_4 and NiO, but it was still very satisfactory [154]. Later, the mechanism of the reaction was explored in Mn_3O_4 nanoparticles (15–45 nm) without additional carbon (no carbon coating and no carbon template) [155]. Firstly, Mn_3O_4 is reduced to MnO together with the formation of Na_2O at ca. 0.6 V, and then to Mn at ca. 0.4 V. During the charge, metallic Mn is reoxidized to MnO at 0.1 V, and to Mn_3O_4 at ca. 0.8 V. The cycling stability is reasonable (158 mAh g^{-1} after 200 cycles).

A microstructure of cubic-like Mn_2O_3 with nanoparticles (sub-units) embedded on its porous surface was obtained. The electrochemical results indicate that the Mn_2O_3 electrode can deliver a promising discharge capacity, cyclability, and rate capability during the (de)insertion of Na-ions. The Mn_2O_3 electrode exhibited a high initial discharge capacity of 544 mAh g^{-1} at 100 mA g^{-1} and retained 130 mAh g^{-1} after 200 cycles [156].

The crystal structure of MnOOH contains tunnels such as β-MnO_2. This manganese oxyhydroxide in the form of nanorods was reported by Shao et al., who surprisingly suggested that MnOOH nanorods undergo a partial conversion to MnO and NaOH in sodium half-cells down to near 0 V [157]:

$$MnOOH + Na^+ + e^- \rightarrow MnO + NaOH \tag{9}$$

During the charging process, MnOOH is regenerated. The reaction allowed a capacity of 421 mAh g^{-1} at 80 mA g^{-1} with 86.7% coulombic efficiency, which is most likely indicative of irreversible processes while the specific capacity was reduced to 162 mAh g^{-1} at 2000 mA g^{-1}.

6.2. Manganese-Based Spinels and Perovskites

The spinels AMn_2O_4 (A = Co) and MnA_2O_4 (A = Fe) have attracted little attention as conversion electrodes for SIB. A main problem for these electrode materials is that the conversion reaction during the first discharge irreversibly consumes sodium, and the initial coulombic efficiency is low.

The composite $MnFe_2O_4$/reduced graphene oxide delivers a stable capacity of 258 mAh g^{-1} at 0.1 C rate for 50 cycles in sodium cells [158]. Fe, Mn, and Na_2O are formed at 0 V through a conversion reaction, while Fe_2O_3 and MnO are detected at the charge state (3.0 V). The graphene sheets enhance the electronic conductivity of the composite, buffer the volume expansion during the conversion reaction, and act as a barrier to avoid active material dissolution. The Na-alginate binder provides strong active material-current collector interaction. Binder-free nanodots of $MnFe_2O_4$ encapsulated in carbon nanofibers, and prepared via the electrospinning method, have particularly good rate-capability and an ultralong cycling life (Figure 14) [159].

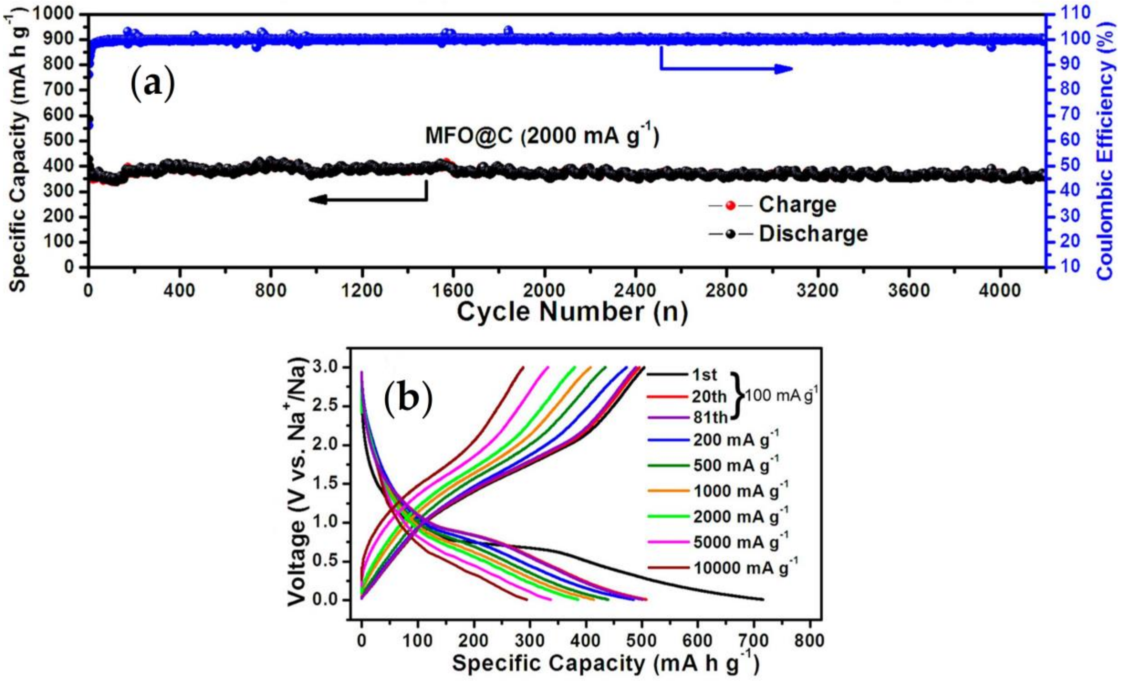

Figure 14. Electrochemical properties of $MnFe_2O_4$@C in sodium cell. Reprinted (adapted) with permission from Ref. [159]. Copyright (2016) ACS.

Yuan et al. used the electrostatic spray deposition technique to fabricate porous $CoMn_2O_4$ on Ni foam, which was proposed as a binder-free electrode [160]. The mechanism for sodium storage is like the lithium conversion mechanism, involving the formation of Co, Mn, and Na_2O at ca. 0 V. The reversible capacity is 185 mAh g^{-1} after 50 cycles at 100 mA g^{-1}.

Fluorides containing Mn and with perovskite-type structures are also under investigation. After introducing K^+ and F^- vacancies in the perovskite-type $KMnF_3$ (s.g. Pm-3m) and the addition of reduced graphene oxide (rGO), the composite $K_{0.86}MnF_{2.69}$@rGO is obtained [161]. Expectedly, the vacancies improve the capacity for sodium intercalation. At about 0.21 V, the fluoride compound is irreversibly converted to Mn metal, KF, and NaF, and the reversible capacity of the composite is only about 40 mAh g^{-1}. The electrochemistry of composites perovskite/reduced graphene oxide electrodes is between sodium-ion batteries and capacitors. The compound $K_{0.71}Ni_{0.12}Co_{0.41}Mn_{0.47}F_{2.77}$ is vacancy defective [162] and, besides the capacity resulting from cationic conversion/intercalation, the anions (e.g., $PF_6{}^-$) in the electrolyte can also be reversibly embedded in the electrode. Yang et al. have very recently reported the perovskite fluoride with nominal composition $K_{0.97}Ni_{0.31}Zn_{0.28}Mn_{0.41}F_{2.}$ [163], and the sodium storage process in this material is based on conversion and alloying (Na-Zn).

7. Methods of Synthesis

Although the one-step solid-state method is often employed for the preparation of many compounds, and these methods are ideal for industrial production, more sophisticated methods are more convenient for fine control of the resulting phases and particle morphology. The preparation of the manganese compounds described above could involve the optimization of the methods of synthesis, particularly for nanostructured materials. The most significant advances in this field are reviewed below. The simplest method to reduce the particle size is ball-milling, but the particles obtained usually have irregular morphologies.

The synthesis based on the sol-gel method and precursor method can be particularly useful for the preparation of nanostructured oxides. New nanosized spinels $Mg_xMn_{2-y}Fe_yO_4$

$(0 \leq y \leq 2)$ were prepared through a modification of the Pechini process [15], firstly dissolving magnesium, manganese, and iron nitrates in water, then adding citric acid and ethylene glycol, and final heating of the resulting precursor. The sol-gel method can be very useful for the cationic substitution in NASICON-type cathodes [164]. Together with citrate precursors, for the synthesis of tunnel-type Na_xMnO_2, the cetyltrimethylammonium bromide (CTAB) surfactant provides a pathway to tailor the particle morphology [53].

Manganese hexacyanomanganate, $Na_2Mn^{II}[Mn^{II}(CN)_6]$, is typically prepared by co-precipitation method, after adding NaCN to an aqueous solution of manganese nitrate in the presence of excess NaCl, and under N_2 atmosphere to avoid oxidation of manganese [127,165]. A much more sophisticated method was employed for the anchoring of $Na_xK_yMnFe(CN)_6$ on hierarchical porous ultrathin carbon networks [166]. This method involves many steps, including the preparation of a template, freeze-drying, and chemical co-precipitation.

The preparation of hollow nanostructures of sodium-manganese compounds for SIB remains little explored, although the recent advances in the preparation of other compounds could be a source of inspiration, for example, the methods based on micelles, solvothermal, and spray-drying [167]. The strategies for the preparation of heterostructures comprise solvothermal/hydrothermal processes, quenching, and other methods [168]. Unfortunately, the methods of preparation of the heterostructures lack the precise control of many properties, such as the interface between the two structures.

8. Conclusions and Perspectives

As a schematic summary, the main advantages and drawbacks are given in Figure 15. Thus, electrode materials made of low-cost elements, such as sodium Na and Mn, are particularly interesting for developing new and sustainable batteries based on green chemistry. Manganese is less toxic than cobalt and nickel. Replacement of lithium by sodium led to avoiding the use of copper in the current collector. These materials could also be adequate for aqueous processing, avoiding organic solvents.

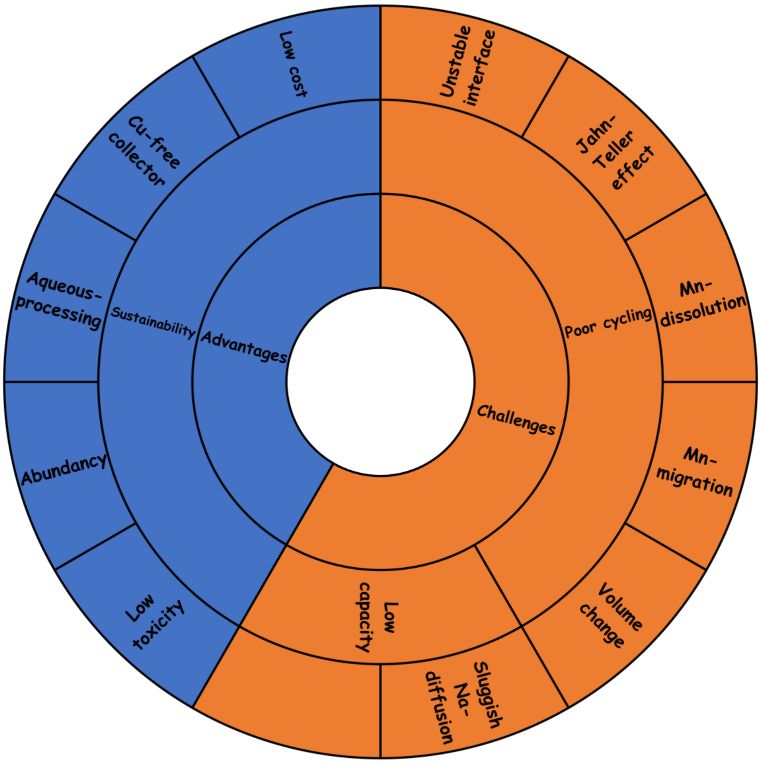

Figure 15. Advantages and challenges of the SIB batteries with manganese compounds.

The main drawback of these insertion-electrode materials is their cycling stability, and the Jahn–Teller effect of manganese is a main contributor to the lack of structural stability. Manganese dissolution has been observed for some electrodes. Compared to layered oxides, the tailoring of the composition to control the structural change during electrochemical cycling has been scarcely explored in non-layered oxides. Spinel-type $NaMn_2O_4$ and tunnel-type $Na_{0.44}MnO_2$ show promise as an efficient and sustainable electrode for SIB, but this material should be tailored to achieve good stability. The possible migration of manganese ions, particularly in the spinel-type structure, could be another source of structural instability. Another main drawback of several of these cathodes, such as the tunnel-type and the spinel-type structure, is the relatively low capacity, particularly at a high rate.

The main strategies to improve the cyclability and increase the energy density of the manganese oxides can be briefly described below and in Figure 16.

- Building biphasic heterostructures, for example, spinel/layered and tunnel/layered. A synergistic effect could be found for the suitable combinations of two different structures in the same electrode material. For example, the formation of heterostructures or composites could be a strategy to raise the capacity of tunnel-type materials [169];
- Partially replacing atoms (cations and/or anions) or doping to improve structural stability. The large volume expansion/contraction and structure transformation should be avoided, for example suppressing the Jahn–Teller distortion. The partial replacement of the Jahn–Teller ion manganese by non-Jahn–Teller ion can allow to achieve better cycling stability;
- Multianion approach and formation of entatic electrode. For example, partial replacement of O by another anion (fluoride, sulfide, or others) [102]. The coordination of an atom (e.g., sodium and manganese) by different types of anions (e.g., F^-/O^{2-}, S^{2-}/O^{2-} and $PO_4{}^{3-}/F^-$) can exert several beneficial effects. In addition, this sort of anion doping can modify the stoichiometry of the compound (Na/Mn ratio) and raise the capacity;
- Replacing Mn by Ni to rise the operating voltage. The redox pair Ni^{4+}/Ni^{2+} can provide higher voltage than Mn^{4+}/Mn^{3+}, with the consequent higher energy density;
- Implementing theoretical calculations to design the materials with thermodynamic stability and optimized properties. DFT calculations are the main tool for selecting new materials, particularly for future materials based on several types of anions;
- Tailoring the particle morphology for shortening the sodium diffusion pathway, particularly in the crystallographic directions in which the mobility of sodium is low. For example, rod morphology is very promising.
- New additives and coatings for the improvement of the electrolyte and interface properties. This involves not only the SEI formation, but also the improvement of cycling life, thermal stability, and safety [170]. Beyond the typical fluoroethylene carbonate (FEC) additive, and formation of NaF-rich SEI in the anode, the additive for SIB should also improve the electrochemistry of the high-voltage cathode (CEI), but this is still in an initial state of exploration compared to LIB.

Regarding new perspectives, we believe that since the perovskite structure offers many possibilities, there is a chance for tailoring the composition and structure of the Mn-containing perovskites for sodium (de)intercalation, such as lithium in $Li_{0.5}La_{0.5}TiO_3$ [171]. The use of pure manganese oxides as conversion electrodes to replace hard-carbon as negative electrode for SIB is doubtful, due to the difficulties in achieving high coulombic efficiency and extended cycling. However, the composites based on manganese oxides and carbon can (e.g., $MnFe_2O_4$@C) exhibit excellent cycling stability [159].

Figure 16. Strategies for improvement of the SIB batteries with manganese compounds.

The two more promising strategies for future progress are most likely the multianion approach and the improvement of the SEI. The multianion approach could mitigate the changes of the unit cell during charge/discharge, particularly due to the Jahn–Teller effect, and it could improve the mobility of sodium in the host material. On the other hand, the engineering of the interfaces by coating treatment could contribute to improving the SEI stability and cycling stability. Beyond carbon coating, new types of materials for the coating of the electrode should be explored, such as borates.

Manthiram group recently found that the electrochemical performance of the spinel $LiMn_{2-x}Fe_xO_4$ can be greatly improved for materials prepared under oxidative synthesis conditions [172]. The oxygen flow during the synthesis minimizes the oxygen vacancies in the structure of the resulting spinel, and it decreases the surface of the particles. We believe that this strategy should also be explored in sodium-manganese spinels.

A drawback of several of the most significant methods of synthesis is that these are time-consuming and inefficient. It would be necessary to develop new methods of synthesis based on fast procedures and low-energy consumption. For example, ultrafast high-temperature sintering with Joule heating is a promising method that has been applied to NASICON-type solid electrolytes, but it may also be a source of inspiration for electrode materials [173].

Author Contributions: Writing—review and editing, J.L.T., A.M., R.S., C.P.-V., R.A. and P.L.; writing—original draft preparation, R.A. All authors have read and agreed to the published version of the manuscript.

Funding: This research was funded by Junta de Andalucía, research group FQM288, and FEDER Andalucía 2020 contract 1380025-R.

Institutional Review Board Statement: Not applicable.

Informed Consent Statement: Not applicable.

Conflicts of Interest: The authors declare no conflict of interest. The funders had no role in the design of the study; in the collection, analyses, or interpretation of data; in the writing of the manuscript, or in the decision to publish the results.

References

1. Hu, Z.; Gao, S. Upper crustal abundances of trace elements: A revision and update. *Chem. Geol.* **2008**, *253*, 205–221. [CrossRef]
2. Yaroshevsky, A.A. Abundances of chemical elements in the Earth's crust. *Geochem. Int.* **2006**, *44*, 48–55. [CrossRef]
3. Parant, J.P.; Olazcuaga, R.; Devalette, M.; Fouassier, C.; Hagenmuller, P. Sur quelques nouvelles phases de formule Na_xMnO_2 ($x \leq 1$). *J. Solid State Chem.* **1971**, *3*, 1–11. [CrossRef]
4. Mendiboure, A.; Delmas, C.; Hagenmuller, P. Electrochemical intercalation and deintercalation of Na_xMnO_2 bronzes. *J. Solid State Chem.* **1985**, *57*, 323–331. [CrossRef]
5. Hunter, J.C. Preparation of a new crystal form of manganese dioxide: λ-MnO_2. *J. Solid State Chem.* **1981**, *39*, 142–147. [CrossRef]
6. Tarascon, J.M.; Guyomard, D.G.; Wilkens, B.; Mc Kinnon, W.R.; Barboux, P. Chemical and electrochemical insertion of Na into the spinel λ-MnO_2 phase. *Solid State Ion.* **1992**, *57*, 113–120. [CrossRef]
7. Bach, S. Electrochemical Sodium Insertion into MnCo Oxide. *Electrochem. Solid-State Lett.* **1999**, *2*, 545. [CrossRef]
8. Kolli, S.K.; der Ven, A. Controlling the Electrochemical properties of Spinel Intercalation Compounds. *ACS Appl. Energy Mater.* **2018**, *1*, 6833–6839. [CrossRef]
9. Kim, S.; Ma, X.; Ong, S.P.; Ceder, G. A comparison of destabilization mechanisms of the layered Na_xMO_2 and Li_xMO_2 compounds upon alkali de-intercalation. *Phys. Chem. Chem. Phys.* **2012**, *14*, 15571–15578. [CrossRef]
10. Kim, J.R.; Amatucci, G.G. $NaMn_{2-x}Ni_xO_4$ Derived from Mesoporous $LiMn_{2-x}Ni_xO_4$: High-Voltage Spinel Cathode Materials for Na-Ion Batteries. *J. Electrochem. Soc.* **2016**, *163*, A696–A705. [CrossRef]
11. Yabuuchi, N.; Yano, M.; Kuze, S.; Komaba, S. Electrochemical behavior and structural change of spinel-type $Li[Li_xMn_{2-x}]O_4$ ($x = 0$ and 0.2) in sodium cells. *Electrochim. Acta* **2012**, *82*, 296–301. [CrossRef]
12. Tang, M.; Yang, J.; Liu, H.; Chen, X.; Kong, L.; Xu, Z.; Huang, J.; Xia, Y. Spinel-Layered Intergrowth Composite Cathodes for Sodium-Ion Batteries. *ACS Appl. Mater. Interfaces* **2020**, *12*, 45997–46004. [CrossRef] [PubMed]
13. Kataoka, R.; Kitta, M.; Ozaki, H.; Takeichi, N.; Kiyobayashi, T. Spinel manganese oxide: A high capacity positive electrode material for the sodium ion battery. *Electrochim. Acta* **2016**, *212*, 458–464. [CrossRef]
14. Kolli, S.K.; Van der Ven, A. Elucidating the Factors That Cause Cation Diffusion Shutdown in Spinel-Based Electrodes. *Chem. Mater.* **2021**, *33*, 6421–6432. [CrossRef]
15. Medina, A.; Pérez-Vicente, C.; Alcántara, R. Spinel-type $Mg_xMn_{2-y}Fe_yO_4$ as a new electrode for sodium ion batteries. *Electrochim. Acta* **2022**, *421*, 140492. [CrossRef]
16. Mosbah, A.; Verbaere, A.; Tournoux, M. Phases $Li_xMnO_2\lambda$ rattachees au type spinelle. *Mater. Res. Bull.* **1983**, *18*, 1375. [CrossRef]
17. Akimoto, J.; Awaka, J.; Kijima, N.; Takahashi, Y.; Maruta, Y.; Tokiwa, K.; Watanabe, T. High-pressure synthesis and crystal structure analysis of $NaMn_2O_4$ with the calcium ferrite-type structure. *J. Solid State Chem.* **2006**, *179*, 169–174. [CrossRef]
18. Mumme, W.G. The structure of $Na_4Mn_4Ti_5O_{18}$. *Acta Crystallogr. B* **1968**, *24*, 1114–1120. [CrossRef]
19. Yamaura, K.; Huang, Q.; Zhang, L.; Takada, K.; Baba, Y.; Nagai, T.; Matsui, Y.; Kosuda, K.; Takayama-Muromachi, E. Spinel-to-$CaFe_2O_4$-Type Structural Transformation in $LiMn_2O_4$ under High Pressure. *J. Am. Chem. Soc.* **2006**, *128*, 9448. [CrossRef]
20. Liu, X.; Wang, X.; Iyo, A.; Yu, H.; Li, D.; Zhou, H. High stable post-spinel $NaMn_2O_4$ cathode of sodium ion battery. *J. Mater. Chem. A* **2014**, *2*, 14822–14826. [CrossRef]
21. Chiring, A.; Senguttuvan, P. Chemical pressure-stabilized post spinel-$NaMnSnO_4$ as potential cathode for sodium-ion batteries. *Bull. Mater. Sci.* **2020**, *43*, 306. [CrossRef]
22. Doeff, M.M.; Peng, M.Y.; Ma, Y.; De Jonghe, L.C. Orthorhombic Na_xMnO_2 as a Cathode Material for Secondary Sodium and Lithium Polymer Batteries. *J. Electrochem. Soc.* **1994**, *141*, L145–L147. [CrossRef]
23. Sauvage, F.; Laffont, L.; Tarascon, J.-M.; Baudrin, E. Study of the Insertion/Deinsertion Mechanism of Sodium into $Na_{0.44}MnO_2$. *Inorg. Chem.* **2007**, *46*, 3289. [CrossRef] [PubMed]
24. Liang, X.; Kim, H.; Jung, H.; Sun, Y. Lithium-Substituted Tunnel/Spinel Heterostructured Cathode Material for High-Performance Sodium-Ion Batteries. *Adv. Funct. Mater.* **2021**, *31*, 2008569. [CrossRef]
25. Kim, H.; Kim, D.J.; Seo, D.-H.; Yeom, M.S.; Kang, K.; Kim, D.K.; Jung, Y. Ab Initio Study of the Sodium Intercalation and Intermediate Phases in $Na_{0.44}$ MnO_2 for Sodium-Ion Battery. *Chem. Mater.* **2012**, *24*, 1205–1211. [CrossRef]
26. Zuo, W.; Qiu, J.; Liu, X.; Zheng, B.; Zhao, Y.; Li, J.; He, H.; Zhou, K.; Xiao, Z.; Li, Q.; et al. Highly-stable P2–$Na_{0.67}MnO_2$ electrode enabled by lattice tailoring and surface engineering. *Energy Storage Mater.* **2020**, *26*, 503. [CrossRef]
27. Kim, H.-J.; Ramasamy, H.V.; Jeong, G.-H.; Aravindan, V.; Lee, Y.-S. Deciphering the Structure–Property Relationship of Na–Mn–Co–Mg–O as a Novel High-Capacity Layered–Tunnel Hybrid Cathode and Its Application in Sodium-Ion Capacitors. *ACS Appl. Mater. Interfaces* **2020**, *12*, 10268. [CrossRef] [PubMed]
28. Doeff, M.M.; Richardson, T.J.; Hwang, K.-T. Electrochemical and structural characterization of titanium-substituted manganese oxides based on $Na_{0.44}MnO_2$. *J. Power Sources* **2004**, *135*, 240–248. [CrossRef]

29. Wang, Y.; Liu, J.; Lee, B.; Qiao, R.; Yang, Z.; Xu, S.; Yu, X.; Gu, L.; Hu, Y.-S.; Yang, W.; et al. Ti-substituted tunnel-type $Na_{0.44}MnO_2$ oxide as a negative electrode for aqueous sodium-ion batteries. *Nat. Commun.* **2015**, *6*, 6401. [CrossRef]
30. Shi, W.-J.; Zhang, D.; Meng, X.-M.; Bao, C.-X.; Xu, S.-D.; Chen, L.; Wang, X.-M.; Liu, S.-B.; Wu, Y.-C. Low-Strain Reticular Sodium Manganese Oxide as an Ultrastable Cathode for Sodium-Ion Batteries. *ACS Appl. Mater. Interfaces* **2020**, *12*, 14174–14184. [CrossRef]
31. Jia, S.; Yao, E.; Peng, R.; Jonderian, A.; Abdolhosseini, M.; McCalla, E. Chemical Speed Dating: The Impact of 52 Dopants in Na–Mn–O Cathodes. *Chem. Mater.* **2022**, *34*, 11047–11061. [CrossRef]
32. Xu, S.; Wang, Y.; Ben, L.; Lyu, Y.; Song, N.; Yang, Z.; Li, Y.; Mu, L.; Yang, H.-T.; Gu, L.; et al. Fe-Based Tunnel-Type $Na_{0.61}[Mn_{0.27}Fe_{0.34}Ti_{0.39}]O_2$ Designed by a New Strategy as a Cathode Material for Sodium-Ion Batteries. *Adv. Energy Mater.* **2015**, *5*, 1501156. [CrossRef]
33. Zhong, W.; Huang, Q.; Zheng, F.; Deng, Q.; Pan, Q.; Liu, Y.; Li, Y.; Li, Y.; Hu, J.; Yang, C.; et al. Structural Insight into the Abnormal Capacity of a Co-Substituted Tunnel-Type $Na_{0.44}MnO_2$ Cathode for Sodium-Ion Batteries. *ACS Appl. Mater. Interfaces* **2020**, *12*, 47548–47555. [CrossRef] [PubMed]
34. Han, D.-W.; Ku, J.-H.; Kim, R.-H.; Yun, D.-J.; Lee, S.-S.; Doo, S.-G. Aluminum Manganese Oxides with Mixed Crystal Structure: High-Energy-Density Cathodes for Rechargeable Sodium Batteries. *ChemSusChem* **2014**, *7*, 1870–1875. [CrossRef] [PubMed]
35. Fu, B.; Zhou, X.; Wang, Y. High-rate performance electrospun $Na_{0.44}MnO_2$ nanofibers as cathode material for sodium-ion batteries. *J. Power Sources* **2016**, *310*, 102. [CrossRef]
36. Liu, Q.; Hu, Z.; Chen, M.; Gu, Q.; Dou, Y.; Sun, Z.; Chou, S.; Dou, S.X. Multiangular Rod-Shaped $Na_{0.44}MnO_2$ as Cathode Materials with High Rate and Long Life for Sodium-Ion Batteries. *ACS Appl. Mater. Interfaces* **2017**, *9*, 3644–3652. [CrossRef] [PubMed]
37. Dai, K.; Mao, J.; Song, X.; Battaglia, V.; Liu, G. $Na_{0.44}MnO_2$ with very fast sodium diffusion and stable cycling synthesized via polyvinylpyrrolidone-combustion method. *J. Power Sources* **2015**, *285*, 161–168. [CrossRef]
38. He, X.; Wang, J.; Qiu, B.; Paillard, E.; Ma, C.; Cao, X.; Liu, H.; Stan, M.C.; Liu, H.; Gallash, T.; et al. Durable high-rate capability $Na_{0.44}MnO_2$ cathode material for sodium-ion batteries. *Nano Energy* **2016**, *27*, 602–610. [CrossRef]
39. Dall'Asta, V.; Buchholz, D.; Chagas, L.G.; Dou, X.; Ferrara, C.; Quartarone, E.; Tealdi, C.; Passerini, S. Aqueous Processing of $Na_{0.44}MnO_2$ Cathode Material for the Development of Greener Na-Ion Batteries. *ACS Appl. Mater. Interfaces* **2017**, *9*, 34891–34899. [CrossRef]
40. Jo, J.H.; Choi, J.U.; Park, Y.J.; Ko, J.K.; Yashiro, H.; Myung, S.-T. A new pre-sodiation additive for sodium-ion batteries. *Energy Storage Mater.* **2020**, *32*, 281–289. [CrossRef]
41. Ferrara, C.; Tealdi, C.; Dall'Asta, V.; Buchholz, D.; Chagas, L.; Quartarone, E.; Berbenni, V.; Passerini, S. High-Performance $Na_{0.44}MnO_2$ Slabs for Sodium-Ion Batteries Obtained through Urea-Based Solution Combustion Synthesis. *Batteries* **2018**, *4*, 8. [CrossRef]
42. Choi, J.U.; Jo, J.H.; Jo, C.-H.; Cho, M.K.; Park, Y.J.; Jin, Y.; Yashiro, H.; Myung, S.-T. Impact of Na_2MoO_4 nanolayers autogenously formed on tunnel-type $Na_{0.44}MnO_2$. *J. Mater. Chem. A Mater.* **2019**, *7*, 13522–13530. [CrossRef]
43. Tevar, A.D.; Whitacre, J.F. Relating Synthesis Conditions and Electrochemical Performance for the Sodium Intercalation Compound $Na_4Mn_9O_{18}$ in Aqueous Electrolyte. *J. Electrochem. Soc.* **2010**, *157*, A870. [CrossRef]
44. Rim, C.-H.; Jang, C.-H.; Kim, K.-H.; Ryu, C.; Yu, C.-J. Point defects and their impact on electrochemical performance in $Na_{0.44}MnO_2$ for sodium-ion battery cathode application. *Phys. Chem. Chem. Phys.* **2022**, *24*, 22736–22745. [CrossRef] [PubMed]
45. de Boisse, B.M.; Nishimura, S.; Watanabe, E.; Lander, L.; Tsuchimoto, A.; Kikkawa, J.; Kobayashi, E.; Asakura, D.; Okubo, M.; Yamada, A. Highly Reversible Oxygen-Redox Chemistry at 4.1 V in $Na_{4/7-x}[\square_{1/7}Mn_{6/7}]O_2$ (□: Mn Vacancy). *Adv Energy Mater.* **2018**, *8*, 1800409. [CrossRef]
46. Song, B.; Tang, M.; Hu, E.; Borkiewicz, O.J.; Wiaderek, K.M.; Zhang, Y.; Phillip, N.D.; Liu, X.; Shadike, Z.; Li, C.; et al. Understanding the Low-Voltage Hysteresis of Anionic Redox in $Na_2Mn_3O_7$. *Chem. Mater.* **2019**, *31*, 3756–3765. [CrossRef]
47. Li, Y.; Wang, X.; Gao, Y.; Zhang, Q.; Tan, G.; Kong, Q.; Bak, S.; Lu, G.; Yang, X.; Gu, L.; et al. Native Vacancy Enhanced Oxygen Redox Reversibility and Structural Robustness. *Adv. Energy Mater.* **2019**, *9*, 1803087. [CrossRef]
48. Wang, Q.; Yang, W.; Kang, F.; Li, B. $Na_2Mn^{3+}{}_{0.3}Mn^{4+}{}_{2.7}O_{6.85}$: A cathode with simultaneous cationic and anionic redox in Na-ion battery. *Energy Storage Mater.* **2018**, *14*, 361–366. [CrossRef]
49. Adamczyk, E.; Pralong, V. $Na_2Mn_3O_7$: A Suitable Electrode Material for Na-Ion Batteries? *Chem. Mater.* **2017**, *29*, 4645–4648. [CrossRef]
50. Zheng, P.; Su, J.; Wang, Y.; Zhou, W.; Song, J.; Su, Q.; Reeves-McLaren, N.; Guo, S. A High-Performance Primary Nanosheet Heterojunction Cathode Composed of $Na_{0.44}MnO_2$ Tunnels and Layered $Na_2Mn_3O_7$ for Na-Ion Batteries. *ChemSusChem* **2020**, *13*, 1793–1799. [CrossRef]
51. Li, X.; Bao, J.; Li, Y.; Chen, D.; Ma, C.; Qiu, Q.; Yue, X.; Wang, Q.; Zhou, Y. Boosting Reversibility of Mn-Based Tunnel-Structured Cathode Materials for Sodium-Ion Batteries by Magnesium Substitution. *Adv. Sci.* **2021**, *8*, 2004448. [CrossRef] [PubMed]
52. Chen, J.; Hou, Z.; Zhang, L.; Mao, W.; Zhang, T.; Zhang, X.; Qian, Y. An advanced medium-entropy substituted tunnel-type $Na_{0.44}MnO_2$ cathode for high-performance sodium-ion batteries. *Inorg. Chem. Front.* **2023**, *10*, 841–849. [CrossRef]
53. Zhang, J.; Yuan, H.; Huang, Y.; Kan, S.; Wu, Y.; Bu, M.; Liu, Y.; He, P.; Liu, H. Engineering sodium-rich manganese oxide with robust tunnel structure for high-performance sodium-ion battery cathode application. *Chem. Eng. J.* **2021**, *417*, 128097. [CrossRef]

54. Pandit, B.; Rondiya, S.R.; Dzade, N.Y.; Shaikh, S.F.; Kumar, N.; Goda, E.S.; Al-Kahtani, A.A.; Mane, R.S.; Mathur, S.; Salunkhe, R.R. High Stability and Long Cycle Life of Rechargeable Sodium-Ion Battery Using Manganese Oxide Cathode: A Combined Density Functional Theory (DFT) and Experimental Study. *ACS Appl. Mater. Interfaces* **2021**, *13*, 11433–11441. [CrossRef] [PubMed]
55. Zhang, Z.; Zhao, X.; Li, J. Facile Synthesis of Nanostructured MnO_2 as Anode Materials for Sodium-Ion Batteries. *ChemNanoMat* **2016**, *2*, 196–200. [CrossRef]
56. Tompsett, D.A.; Islam, M.S. Electrochemistry of Hollandite α-MnO_2: Li-Ion and Na-Ion Insertion and Li_2O Incorporation. *Chem. Mater.* **2013**, *25*, 2515–2526. [CrossRef]
57. Rossouw, M.H.; Liles, D.C.; Thackeray, M.; David, W.I.F.; Hull, S. Alpha manganese dioxide for lithium batteries: A structural and electrochemical study. *Mater. Res. Bull.* **1992**, *27*, 221–230. [CrossRef]
58. Meenakshi Sundaram, K. Catalyst effectiveness factor for Langmuir-Hinshelwood-Hougen-Watson kinetic expressions. *Chem. Eng. Commun.* **1982**, *15*, 305–311. [CrossRef]
59. Sato, T.; Sato, K.; Zhao, W.; Kajiya, Y.; Yabuuchi, N. Metastable and nanosize cation-disordered rocksalt-type oxides: Revisit of stoichiometric $LiMnO_2$ and $NaMnO_2$. *J. Mater. Chem. A* **2018**, *6*, 13943–13951. [CrossRef]
60. Pompa, F.; Siciliano, F. Distorsioni cristallografiche nelle strutture A B F3. Nota I: Struttura cristallina di $NaMnF_3$. *Ric. Sci.* **1969**, *39*, 21–34.
61. Li, H.; Liu, A.; Zhao, S.; Guo, Z.; Wang, N.; Ma, T. In Situ Growth of a Feather-like MnO_2 Nanostructure on Carbon Paper for High-Performance Rechargeable Sodium-Ion Batteries. *ChemElectroChem* **2018**, *5*, 3266–3272. [CrossRef]
62. Huang, J.; Poyraz, A.S.; Lee, S.-Y.; Wu, L.; Zhu, Y.; Marschilok, A.C.; Takeuchi, K.J.; Takeuchi, E.S. Silver-Containing α-MnO_2 Nanorods: Electrochemistry in Na-Based Battery Systems. *ACS Appl. Mater. Interfaces* **2017**, *9*, 4333–4342. [CrossRef] [PubMed]
63. Su, D.; Ahn, H.-J.; Wang, G. Hydrothermal synthesis of α-MnO_2 and β-MnO_2 nanorods as high capacity cathode materials for sodium ion batteries. *J. Mater. Chem. A* **2013**, *1*, 4845–4850. [CrossRef]
64. Su, D.; Ahn, H.-J.; Wang, G. β-MnO_2 nanorods with exposed tunnel structures as high-performance cathode materials for sodium-ion batteries. *NPG Asia Mater.* **2013**, *5*, e70. [CrossRef]
65. Zhou, Y.; Chen, T.; Zhang, J.; Liu, Y.; Ren, P. Amorphous MnO_2 as Cathode Material for Sodium-ion Batteries. *Chin. J. Chem.* **2017**, *35*, 1294–1298. [CrossRef]
66. Kim, J.R.; Amatucci, G.G. Structural and Electrochemical Investigation of Na+ Insertion into High-Voltage Spinel Electrodes. *Chem. Mater.* **2015**, *27*, 2546–2556. [CrossRef]
67. Kim, H.; Kim, D.; Cho, M. Chemomechanical Design Factors for High Performance in Manganese-Based Spinel Cathode Materials for Advanced Sodium-Ion Batteries. *ACS Appl. Mater. Interfaces* **2020**, *12*, 22789–22797. [CrossRef]
68. Kim, H.; Kim, M.; Kim, D.; Cho, M. Physicochemical Design Principles Enabling High-Energy and -Power Low-Cost Na Storage Materials. *J. Phys. Chem. C* **2021**, *125*, 3305–3313. [CrossRef]
69. Alcántara, R.; Jaraba, M.; Lavela, P.; Tirado, J.L.; Biensan, P.; de Guibert, A.; Jordy, C.; Peres, J.P. Structural and Electrochemical Study of New $LiNi_{0.5}Ti_xMn_{1.5-x}O_4$ Spinel Oxides for 5-V Cathode Materials. *Chem. Mater.* **2003**, *15*, 2376–2382. [CrossRef]
70. Sato, K.; Nakayama, M.; Glushenkov, A.M.; Mukai, T.; Hashimoto, Y.; Yamanaka, K.; Yoshimura, M.; Ohta, T.; Yabuuchi, N. Na-Excess Cation-Disordered Rocksalt Oxide: $Na_{1.3}Nb_{0.3}Mn_{0.4}O_2$. *Chem. Mater.* **2017**, *29*, 5043–5047. [CrossRef]
71. Kobayashi, T.; Zhao, W.; Rajendra, H.B.; Yamanaka, K.; Ohta, T.; Yabuuchi, N. Nanosize Cation-Disordered Rocksalt Oxides: Na_2TiO_3–$NaMnO_2$ Binary System. *Small* **2020**, *16*, 1902462. [CrossRef] [PubMed]
72. Takada, T.; Hayakawa, H.; Akiba, E.; Izumi, F.; Chakoumakos, B.C. Novel synthesis process and structure refinements of $Li_4Mn_5O_{12}$ for rechargeable lithium batteries. *J. Power Sources* **1997**, *68*, 613–617. [CrossRef]
73. Zhang, J.; Wang, W.; Li, Y.; Denis, Y.W. Sodium storage capability of spinel $Li_4Mn_5O_{12}$. *Electrochim. Acta* **2015**, *185*, 76–82. [CrossRef]
74. Jo, M.R.; Kim, Y.; Yang, J.; Jeong, M.; Song, K.; Kim, Y.-I.; Lim, J.-M.; Cho, M.; Shim, J.-H.; Kim, Y.-M.; et al. Triggered reversible phase transformation between layered and spinel structure in manganese-based layered compounds. *Nat. Commun.* **2019**, *10*, 3385. [CrossRef] [PubMed]
75. Sun, X.; Duffort, V.; Mehdi, B.L.; Browning, N.D.; Nazar, L.F. Investigation of the Mechanism of Mg Insertion in Birnessite in Nonaqueous and Aqueous Rechargeable Mg-Ion Batteries. *Chem. Mater.* **2016**, *28*, 534–542. [CrossRef]
76. Nam, K.W.; Kim, S.; Yang, E.; Jung, Y.; Levi, E.; Aurbach, D.; Choi, J.W. Critical Role of Crystal Water for a Layered Cathode Material in Sodium Ion Batteries. *Chem. Mater.* **2015**, *27*, 3721–3725. [CrossRef]
77. Zhu, K.; Guo, S.; Li, Q.; Weis, Y.; Chen, G.; Zhou, H. Tunable Electrochemistry via Controlling Lattice Water in Layered Oxides of Sodium-Ion Batteries. *ACS Appl. Mater. Interfaces* **2017**, *9*, 34909–34914. [CrossRef]
78. Michail, A.; Silván, B.; Tapia-Ruiz, N. Progress in high-voltage $MgMn_2O_4$ oxyspinel cathode material for Mg batteries. *Curr. Opin. Electrochem.* **2022**, *31*, 100817. [CrossRef]
79. Montalbano, M.; Callegari, D.; Tamburini, U.A.; Tealdi, C. Design of Perovskite-Type Fluorides Cathodes for Na-ion Batteries: Correlation between Structure and Transport. *Batteries* **2022**, *8*, 126. [CrossRef]
80. Nava-Avendaño, J.; Dompablo, M.E.A.-D.; Frontera, C.; Ayllón, J.A.; Palacín, M.R. Study of sodium manganese fluorides as positive electrodes for Na-ion batteries. *Solid State Ion.* **2015**, *278*, 106–113. [CrossRef]
81. Kitajou, A.; Ishado, Y.; Yamashita, T.; Momida, H.; Oguchi, T.; Okada, S. Cathode Properties of Perovskite-type $NaMF_3$ (M = Fe, Mn, and Co) Prepared by Mechanical Ball Milling for Sodium-ion Battery. *Electrochim. Acta* **2017**, *245*, 424–429. [CrossRef]

82. Moghadam, Y.S.; El Kharbachi, A.; Hu, Y.; Wang, K.; Belin, S.; Fichtner, M. Na-Rich Disordered Rock Salt Oxyfluoride Cathode Materials for Sodium Ion Batteries. *ACS Mater. Lett.* **2023**, *5*, 125–132. [CrossRef]
83. Zan, F.; Yao, Y.; Savilov, S.V.; Suslova, E.; Xia, H. Layered-tunnel structured cathode for high performance sodium-ion batteries. *Funct. Mater. Lett.* **2020**, *13*, 2051016. [CrossRef]
84. Chae, M.S.; Kim, H.J.; Lyoo, J.; Attias, R.; Gofer, Y.; Hong, S.; Aurbach, D. Anomalous Sodium Storage Behavior in Al/F Dual-Doped P2-Type Sodium Manganese Oxide Cathode for Sodium-Ion Batteries. *Adv. Energy Mater.* **2020**, *10*, 2002205. [CrossRef]
85. Wang, Q.-C.; Qiu, Q.-Q.; Xiao, N.; Fu, Z.-W.; Wu, X.-J.; Yang, X.-Q.; Zhou, Y.-N. Tunnel-structured $Na_{0.66}[Mn_{0.66}Ti_{0.34}]O_{2-x}F$ (x < 0.1) cathode for high performance sodium-ion batteries. *Energy Storage Mater.* **2018**, *15*, 1–7. [CrossRef]
86. Boyadzhieva, T.; Koleva, V.; Kukeva, R.; Nihtianova, D.; Harizanova, S.; Stoyanova, R. Storage performance of Mg^{2+} substituted $NaMnPO_4$ with an olivine structure. *RSC Adv.* **2020**, *10*, 29051–29060. [CrossRef] [PubMed]
87. Morgan, D.; Van der Ven, A.; Ceder, G. Li Conductivity in Li_xMPO_4 (M = Mn, Fe, Co, Ni) Olivine Materials. *Electrochem. Solid-State Lett.* **2004**, *7*, A30–A32. [CrossRef]
88. Ong, S.P.; Chevrier, V.L.; Hautier, G.; Jain, A.; Moore, C.; Kim, S.; Ma, X.; Ceder, G. Voltage, stability and diffusion barrier differences between sodium-ion and lithium-ion intercalation materials. *Energy Environ. Sci.* **2011**, *4*, 3680–3688. [CrossRef]
89. Venkatachalam, P.; Ganesan, S.; Rengapillai, S.; Marimuthu, S. Gradual Development of Maricite $NaMnPO_4$ with the Influence of Diol Chain Length on the Polyol Process of Surpassed Sodium Intercalation. *Ind. Eng. Chem. Res.* **2021**, *60*, 5861–5868. [CrossRef]
90. Dima, R.S.; Maleka, P.M.; Maluta, E.N.; Maphanga, R.R. First principles study on sodium de-intercalation from $NaMnPO_4$. *Mater. Today Proc.* **2022**, *62*, S7–S11. [CrossRef]
91. Boyadzhieva, T.; Koleva, V.; Zhecheva, E.; Nihtianova, D.; Mihaylov, L.; Stoyanova, R. Competitive lithium and sodium intercalation into sodium manganese phospho-olivine $NaMnPO_4$ covered with carbon black. *RSC Adv.* **2015**, *5*, 87694–87705. [CrossRef]
92. Sukkabot, W. Tailoring doping effect in olivine-type $NaMnPO_4$: Insights from density functional theory. *Phys. Scr.* **2020**, *95*, 065804. [CrossRef]
93. Yakubovich, O.V.; Karimova, O.V.; Mel'nikov, O.K. The Mixed Anionic Framework in the Structure of $Na_2\{MnF[PO_4]\}$. *Acta Crystallogr. C Struct. Chem.* **1997**, *53*, 395–397. [CrossRef]
94. Wu, X.; Zheng, J.; Gong, Z.; Yang, Y. Sol–gel synthesis and electrochemical properties of fluorophosphates $Na_2Fe_{1-x}Mn_xPO_4F/C$ (x = 0, 0.1, 0.3, 0.7, 1) composite as cathode materials for lithium ion battery. *J. Mater. Chem.* **2011**, *21*, 18630–18637. [CrossRef]
95. Xie, Y.; Wang, H.; Liu, R.; Wang, Z.; Wen, W.; Jiang, Z.; Gong, Z.; Yang, Y. In Situ Monitoring of Structural and Valence Evolution during Electrochemical Desodiation/Sodiation Process of $Na_2Fe_{0.5}Mn_{0.5}PO_4F$. *J. Electrochem. Soc.* **2017**, *164*, A3487–A3492. [CrossRef]
96. Kim, S.-W.; Seo, D.-H.; Kim, H.; Park, K.-Y.; Kang, K. A comparative study on Na_2MnPO_4F and Li_2MnPO_4F for rechargeable battery cathodes. *Phys. Chem. Chem. Phys.* **2012**, *14*, 3299–3303. [CrossRef] [PubMed]
97. Hautier, G.; Jain, A.; Chen, H.; Moore, C.; Ong, S.P.; Ceder, G. Novel mixed polyanions lithium-ion battery cathode materials predicted by high-throughput ab initio computations. *J. Mater. Chem.* **2011**, *21*, 17147–17153. [CrossRef]
98. Chen, H.; Hautier, G.; Ceder, G. Synthesis, Computed Stability, and Crystal Structure of a New Family of Inorganic Compounds: Carbonophosphates. *J. Am. Chem. Soc.* **2012**, *134*, 19619–19627. [CrossRef]
99. Chen., H.; Hao, Q.; Zivkovic, O.; Hautier, G.; Du, L.-S.; Tang, Y.; Hu, Y.-Y.; Ma, X.; Grey, C.P.; Ceder, G. Sidorenkite ($Na_3MnPO_4CO_3$): A New Intercalation Cathode Material for Na-Ion Batteries. *Chem. Mater.* **2013**, *25*, 2777–2786. [CrossRef]
100. Wang, C.; Sawicki, M.; Emani, S.; Liu, C.; Shaw, L.L. $Na_3MnCO_3PO_4$—A High Capacity, Multi-Electron Transfer Redox Cathode Material for Sodium Ion Batteries. *Electrochim. Acta* **2015**, *161*, 322. [CrossRef]
101. Wang, C.; Sawicki, M.; Kaduk, J.A.; Shaw, L.L. Roles of Processing, Structural Defects and Ionic Conductivity in the Electrochemical Performance of $Na_3MnCO_3PO_4$ Cathode Material. *J. Electrochem. Soc.* **2015**, *162*, A1601–A1609. [CrossRef]
102. Vicente, C.P.; Alcántara, R. New perspectives on the multianion approach to adapt the electrode material for lithium and post-lithium batteries. *Phys. Chem. Chem. Phys.* **2023**, *25*, 15600–15623. [CrossRef] [PubMed]
103. Klee, R.; Aragon, M.J.; Lavela, P.; Alcántara, R.; Tirado, J.L. $Na_3V_2(PO_4)_3/C$ nanorods with improved electrode-electrolyte interface as cathode material for sodium-ion batteries. *ACS Appl. Mater. Interfaces* **2016**, *8*, 23151–23159. [CrossRef] [PubMed]
104. Rui, X.; Sun, W.; Wu, C.; Yu, Y.; Yan, Q. An Advanced Sodium-Ion Battery Composed of Carbon Coated $Na_3V_2(PO_4)_3$ in a Porous Graphene Network. *Adv. Mater.* **2015**, *27*, 6670–6676. [CrossRef] [PubMed]
105. Liu, J.; Tang, K.; Song, K.; van Aken, P.A.; Yu, Y.; Maier, J. Electrospun $Na_3V_2(PO_4)_3/C$ nanofibers as stable cathode materials for sodium-ion batteries. *Nanoscale* **2014**, *6*, 5081–5086. [CrossRef]
106. Singh, B.; Wang, Z.; Park, S.; Gautam, G.S.; Chotard, J.; Croguennec, L.; Carlier, D.; Cheetham, A.K.; Masquelier, C.; Canepa, P. A Chemical Map of NaSiCON Electrode Materials for Sodium-ion Batteries. *J. Mater. Chem. A* **2021**, *9*, 281–292. [CrossRef]
107. Zhou, W.; Xue, L.; Lu, X.; Gao, H.; Li, Y.; Xin, S.; Fu, G.; Cui, Z.; Zhu, Y.; Goodenough, J.B. $Na_xMV(PO_4)_3$ (M = Mn, Fe, Ni) structure and properties for sodium extraction. *Nano Lett.* **2016**, *16*, 7836. [CrossRef]
108. Huang, Y.; Li, X.; Wang, J.; Miao, L.; Li, C.; Han, J.; Huang, Y. Superior Na-ion storage achieved by Ti substitution in $Na_3V_2(PO_4)_3$. *Energy Storage Mater.* **2018**, *15*, 108–115. [CrossRef]
109. Gao, H.; Seymour, I.D.; Xin, S.; Xue, L.; Henkelman, G.; Goodenough, J.B. $Na_3MnZ_r(PO_4)_3$: A High-Voltage Cathode for Sodium Batteries. *J. Am. Chem. Soc.* **2018**, *140*, 18192–18199. [CrossRef]

110. Zhu, T.; Hu, P.; Cai, C.; Liu, Z.; Hu, G.; Kuang, Q.; Mai, L.; Zhou, L. Dual carbon decorated $Na_3MnTi(PO_4)_3$: A high-energy-density cathode material for sodium-ion batteries. *Nano Energy* **2020**, *70*, 104548. [CrossRef]
111. Ma, X.; Wu, X.; Liu, Y.; Wu, W.; Pan, Z.; Shen, P.K. Toward a High-Energy-Density Cathode with Enhanced Temperature Adaptability for Sodium-Ion Batteries: A Case Study of $Na_3MnZr(PO_4)_3$ Microspheres with Embedded Dual-Carbon Networks. *ACS Appl. Mater. Interfaces* **2021**, *13*, 21390–21400. [CrossRef] [PubMed]
112. Gao, H.; Li, Y.; Park, K.; Goodenough, J.B. Sodium Extraction from NASICON-Structured $Na_3MnTi(PO_4)_3$ through Mn(III)/Mn(II) and Mn(IV)/Mn(III) Redox Couples. *Chem. Mater.* **2016**, *28*, 6553–6559. [CrossRef]
113. Zhou, Y.; Shao, X.; Lam, K.; Zheng, Y.; Zhao, L.; Wang, K.; Zhao, J.; Chen, F.; Hou, X. Symmetric Sodium-Ion Battery Based on Dual-Electron Reactions of NASICON-Structured $Na_3MnTi(PO_4)_3$ Material. *ACS Appl. Mater. Interfaces* **2020**, *12*, 30328–30335. [CrossRef] [PubMed]
114. Li, H.; Xu, M.; Gao, C.; Zhang, W.; Zhang, Z.; Lai, Y.; Jiao, L. Highly efficient, fast and reversible multi-electron reaction of $Na_3MnTi(PO_4)_3$ cathode for sodium-ion batteries. *Energy Storage Mater.* **2020**, *26*, 325–333. [CrossRef]
115. Li, H.; Zhang, W.; Han, Z.; Sun, K.; Gao, C.; Cheng, K.; Liu, Z.; Chen, Q.; Zhang, J.; Lai, Y.; et al. Pseudocapacitance enhanced by N-defects in $Na_3MnTi(PO_4)_3$/N-doped carbon composite for symmetric full sodium-ion batteries. *Mater. Today Energy* **2021**, *21*, 100754. [CrossRef]
116. Zhang, J.; Liu, Y.; Zhao, X.; He, L.; Liu, H.; Song, Y.; Sun, S.; Li, Q.; Xing, X.; Chen, J. A novel NASICON-type $Na_4MnCr(PO_4)_3$ demonstrating the energy density record of phosphate cathodes for sodium-ion batteries. *Adv Mater.* **2020**, *32*, 1906348. [CrossRef] [PubMed]
117. Lavela, P.; Klee, R.; Tirado, J.L. On the benefits of Cr substitution on $Na_4MnV(PO_4)_3$ to improve the high voltage performance as cathode for sodium-ion batteries. *J. Power Sources* **2021**, *495*, 229811. [CrossRef]
118. Klee, R.; Lavela, P.; Tirado, J.L. Effect of the Mn/V ratio to optimize the kinetic properties of $Na_{3+x}Mn_xV_{1-x}Cr(PO_4)_3$ positive electrode for sodium-ion batteries. *Electrochim. Acta* **2021**, *375*, 137982. [CrossRef]
119. Zheng, Y.; Liu, J.; Huang, D.; Chen, H.; Hou, X. Prepare and optimize NASICON-type $Na_4MnAl(PO_4)_3$ as low cost cathode for sodium ion batteries. *Surf. Interfaces* **2022**, *32*, 102151. [CrossRef]
120. Chen, C.-Y.; Matsumoto, K.; Nohira, T.; Hagiwara, R. Na_2MnSiO_4 as a positive electrode material for sodium secondary batteries using an ionic liquid electrolyte. *Electrochem. Commun.* **2014**, *45*, 63–66. [CrossRef]
121. Law, M.; Ramar, V.; Balaya, P. Na_2MnSiO_4 as an attractive high capacity cathode material for sodium-ion battery. *J. Power Sources* **2017**, *359*, 277–284. [CrossRef]
122. Zhang, P.; Xu, Y.; Zheng, F.; Wu, S.Q.; Yang, Y.; Zhu, Z.-Z. Ion diffusion mechanism in Pn $Na_xLi_{2-x}MnSiO_4$. *CrystEngComm* **2015**, *17*, 2123–2128. [CrossRef]
123. Kuganathan, A. Chroneos, Defects, Dopants and Sodium Mobility in Na_2MnSiO_4. *Sci. Rep.* **2018**, *8*, 14669. [CrossRef]
124. Wang, L.; Lu, Y.; Liu, J.; Xu, M.; Cheng, J.; Zhang, D.; Goodenough, J.B. A Superior Low-Cost Cathode for a Na-Ion Battery. *Angew. Chem. Int. Ed.* **2013**, *52*, 1964–1967. [CrossRef] [PubMed]
125. Qian, J.; Wu, C.; Cao, Y.; Ma, Z.; Huang, Y.; Ai, X.; Yang, H. Prussian Blue Cathode Materials for Sodium-Ion Batteries and Other Ion Batteries. *Adv. Energy Mater.* **2018**, *8*, 1702619. [CrossRef]
126. Kareis, C.M.; Lapidus, S.H.; Her, J.-H.; Stephens, P.W.; Miller, J.S. Non-Prussian Blue Structures and Magnetic Ordering of $Na_2Mn^{II}[Mn^{II}(CN)_6]$ and $Na_2Mn^{II}[Mn^{II}(CN)_6]\cdot 2H_2O$. *J. Am. Chem. Soc.* **2012**, *134*, 2246–2254. [CrossRef] [PubMed]
127. Lee, H.-W.; Wang, R.Y.; Pasta, M.; Lee, S.W.; Liu, N.; Cui, Y. Manganese hexacyanomanganate open framework as a high-capacity positive electrode material for sodium-ion batteries. *Nat. Commun.* **2014**, *5*, 5280. [CrossRef] [PubMed]
128. Hurlbutt, K.; Giustino, F.; Volonakis, G.; Pasta, M. Origin of the High Specific Capacity in Sodium Manganese Hexacyanomanganate. *Chem. Mater.* **2022**, *34*, 4336–4343. [CrossRef]
129. Yang, D.; Xu, J.; Liao, X.-Z.; He, Y.-S.; Liu, H.; Ma, Z.-F. Structure optimization of Prussian blue analogue cathode materials for advanced sodium ion batteries. *Chem. Commun.* **2014**, *50*, 13377–13380. [CrossRef]
130. Ma, Y.; Hu, Y.; Pramudya, Y.; Diemant, T.; Wang, Q.; Goonetilleke, D.; Tang, Y.; Zhou, B.; Hahn, H.; Wenzel, W.; et al. Resolving the Role of Configurational Entropy in Improving Cycling Performance of Multicomponent Hexacyanoferrate Cathodes for Sodium-Ion Batteries. *Adv. Funct. Mater.* **2022**, *32*, 220237. [CrossRef]
131. Guo, Y.-D.; Jiang, J.-C.; Xie, J.; Wang, X.; Li, J.-Z.; Wang, D.-H.; Zhou, A.-J. Enhanced performance of core–shell structured sodium manganese hexacyanoferrate achieved by self-limiting Na^+ –Cs^+ ion exchange for sodium-ion batteries. *Rare Met.* **2022**, *41*, 3740–3751. [CrossRef]
132. Zhao, Q.; Wang, W.; Li, Y.; Wu, N.; Guo, Y.; Cheng, W.; Sun, W.; Li, J.; Zhou, A. Ion-exchange surface modification enhances cycling stability and kinetics of sodium manganese hexacyanoferrate cathode in sodium-ion batteries. *Electrochim. Acta* **2021**, *390*, 138842. [CrossRef]
133. Poizot, P.; Laruelle, S.; Grugeon, S.; Dupont, L.; Tarascon, J.-M. Nano-sized transition-metal oxides as negative-electrode materials for lithium-ion batteries. *Nature* **2000**, *407*, 496. [CrossRef] [PubMed]
134. Poizot, P.; Laruelle, S.; Grugeon, S.; Tarascon, J.-M. Rationalization of the Low-Potential Reactivity of 3d-Metal-Based Inorganic Compounds toward Li. *J. Electrochem. Soc.* **2002**, *149*, A1212–A1217. [CrossRef]
135. Alcántara, R.; Jaraba, M.; Lavela, P.; Tirado, J.L.; Jumas, J.C.; Olivier-Fourcade, J. Changes in oxidation state and magnetic order of iron atoms during the electrochemical reaction of lithium with $NiFe_2O_4$. *Electrochem. Commun.* **2003**, *5*, 16–21. [CrossRef]

136. Alcántara, R.; Jaraba, M.; Lavela, P.; Tirado, J.L. New $Ni_xMg_{6-x}MnO_8$ Mixed Oxides as Active Materials for the Negative Electrode of Lithium-Ion Cells. *J. Solid State Chem.* **2002**, *166*, 330–335. [CrossRef]
137. Alcántara, R.; Jaraba, M.; Lavela, P.; Tirado, J.L. $NiCo_2O_4$ Spinel: First Report on a Transition Metal Oxide for the Negative Electrode of Sodium-Ion Batteries. *Chem. Mater.* **2002**, *14*, 2847–2848. [CrossRef]
138. Thissen, A.; Ensling, D.; Madrigal, F.J.F.; Jaegermann, W.; Alcántara, R.; Lavela, P.; Tirado, J.L. Photoelectron Spectroscopic Study of the Reaction of Li and Na with $NiCo_2O_4$. *Chem. Mater.* **2005**, *17*, 5202. [CrossRef]
139. Chadwick, A.V.; Savin, S.L.P.; Fiddy, S.; Alcántara, R.; Lisbona, D.F.; Lavela, P.; Ortiz, G.F.; Tirado, J.L. Formation and Oxidation of Nanosized Metal Particles by Electrochemical Reaction of Li and Na with $NiCo_2O_4$: X-ray Absorption Spectroscopic Study. *J. Phys. Chem. C* **2007**, *111*, 4636. [CrossRef]
140. Aragón, M.J.; León, B.; Vicente, C.P.; Tirado, J.L.; Chadwick, A.V.; Berko, A.; Beh, S.-Y. Cobalt Oxalate Nanoribbons as Negative-Electrode Material for Lithium-Ion Batteries. *Chem. Mater.* **2009**, *21*, 1834–1840. [CrossRef]
141. Aragón, M.J.; León, B.; Serrano, T.; Vicente, C.P.; Tirado, J.L. Synergistic effects of transition metal substitution in conversion electrodes for lithium-ion batteries. *J. Mater. Chem.* **2011**, *21*, 10102. [CrossRef]
142. Zhang, K.; Cui, D.; Huang, X.; Liang, F.; Gao, G.; Song, T.; Zhang, L.; Yao, Y.; Lei, Y. Insights into the interfacial chemistry and conversion mechanism of iron oxalate toward the reduction by lithium. *Chem. Eng. J.* **2021**, *426*, 131446. [CrossRef]
143. Liu, H.; Ding, C.; Dong, Y. Self-Sacrificing Template Synthesis of Micro/Nano Spheres Ni_6MnO_8 as Electrode for High-Performance Lithium-Ion Batteries. *J. Electrochem. Soc.* **2020**, *167*, 110524. [CrossRef]
144. Fang, X.; Lu, X.; Guo, X.; Mao, Y.; Hu, Y.-S.; Wang, J.; Wang, Z.; Wu, F.; Liu, H.; Chen, L. Electrode reactions of manganese oxides for secondary lithium batteries. *Electrochem. Commun.* **2010**, *12*, 1520–1523. [CrossRef]
145. Tsai, Y.-C.; Kuo, C.-T.; Liu, S.-F.; Lee, Y.-T.; Yew, T.-R. Effect of Different Electrolytes on MnO_2 Anodes in Lithium-Ion Batteries. *J. Phys. Chem. C* **2021**, *125*, 1221–1233. [CrossRef]
146. Alcántara, R.; Jaraba, M.; Lavela, P.; Tirado, J.L.; Jumas, J.C.; Olivier-Fourcade, J. Electrochemical lithium reaction of some first-row transition-metal spinel mixed-oxides. In Proceedings of the 202nd Meeting of the Electrochemical Society, Salt Lake City, UT, USA, 20–24 October 2002; Volume 2002-2.
147. López, M.C.; Lavela, P.; Ortiz, G.F.; Tirado, J.L. Transition metal oxide thin films with improved reversibility as negative electrodes for sodium-ion batteries. *Electrochem. Commun.* **2013**, *27*, 152–155. [CrossRef]
148. López, M.C.; Aragón, M.J.; Ortiz, G.F.; Lavela, P.; Alcántara, R.; Tirado, J.L. High Performance Full Sodium-Ion Cell Based on a Nanostructured Transition Metal Oxide as Negative Electrode. *Chem. Eur. J.* **2015**, *21*, 14879–14885. [CrossRef] [PubMed]
149. CJo, H.; Yashiro, H.; Yuan, S.; Shi, L.; Myung, S.-T. Conversion Chemistry of Cobalt Oxalate for Sodium Storage. *ACS Appl. Mater. Interfaces* **2018**, *10*, 40523–40530. [CrossRef]
150. Li, L.; Zheng, Y.; Zhang, S.; Yang, J.; Shao, Z.; Guo, Z. Recent progress on sodium ion batteries: Potential high-performance anodes. *Energy Environ. Sci.* **2018**, *11*, 2310–2340. [CrossRef]
151. Chen, T.; Wu, Z.; Xiang, W.; Wang, E.; Chen, T.; Guo, X.; Chen, Y.; Zhong, B. Cauliflower-like MnO@C/N composites with multiscale, expanded hierarchical ordered structures as electrode materials for Lithium- and Sodium-ion batteries. *Electrochim. Acta* **2017**, *246*, 931–940. [CrossRef]
152. He, Y.; Xu, P.; Zhang, B.; Du, Y.; Song, B.; Han, X.; Peng, H. Ultrasmall MnO Nanoparticles Supported on Nitrogen-Doped Carbon Nanotubes as Efficient Anode Materials for Sodium Ion Batteries. *ACS Appl. Mater. Interfaces* **2017**, *9*, 38401–38408. [CrossRef] [PubMed]
153. Sun, Y.-N.; Yang, L.; Sui, Z.-Y.; Zhao, L.; Goktas, M.; Zhou, H.-Y.; Xiao, P.-W.; Adelhelm, P.; Han, B.-H. Synthesis and thermodynamic investigation of MnO nanoparticle anchored N-doped porous carbon as the anode for Li-ion and Na-ion batteries. *Mater. Chem. Front.* **2019**, *3*, 2728. [CrossRef]
154. Jiang, Y.; Hu, M.; Zhang, D.; Yuan, T.; Sun, W.; Xu, B.; Yan, M. Transition metal oxides for high performance sodium ion battery anodes. *Nano Energy* **2014**, *5*, 60–66. [CrossRef]
155. Yusoff, N.F.M.; Idris, N.H.; Din, M.F.M.; Majid, S.R.; Harun, N.A.; Rahman, M.M. Electrochemical Sodiation/Desodiation into Mn_3O_4 Nanoparticles. *ACS Omega* **2020**, *5*, 29158–29167. [CrossRef] [PubMed]
156. Yusoff NF, M.; Idris, N.H.; Din MF, M.; Majid, S.R.; Harun, N.A.; Rahman, M.M. Investigation on the Electrochemical Performances of Mn_2O_3 as a Potential Anode for Na-Ion Batteries. *Sci. Rep.* **2020**, *10*, 9207–9217. [CrossRef] [PubMed]
157. Shao, L.; Zhao, Q.; Chen, J. MnOOH nanorods as high-performance anodes for sodium ion batteries. *Chem. Commun.* **2017**, *53*, 2435. [CrossRef] [PubMed]
158. Kollu, P.; Kumar, P.R.; Santosh, C.; Kim, D.K.; Grace, A.N. A high capacity $MnFe_2O_4$/rGO nanocomposite for Li and Na-ion battery applications. *RSC Adv.* **2015**, *5*, 63304–63310. [CrossRef]
159. Liu, Y.; Zhang, N.; Yu, C.; Jiao, L.; Chen, J. $MnFe_2O_4$@C Nanofibers as High-Performance Anode for Sodium-Ion Batteries. *Nano Lett.* **2016**, *16*, 3321–3328. [CrossRef]
160. Yuan, J.; Hao, Y.; Chen, C.; Zhang, X.; Wang, C.; Li, X.; Li, Q.; Zhong, G.; Xie, Y. Synthesis of $CoMn_2O_4$ thin films on Ni foams by electrostatic spray deposition as anodes for sodium–ion batteries. *J. Mater. Sci. Mater. Electron.* **2018**, *29*, 11404–11408. [CrossRef]
161. Huang, Y.; Ding, R.; Ying, D.; Yan, T.; Huang, Y.; Tan, C.; Sun, X.; Gao, P.; Liu, E. Vacant Manganese-Based Perovskite Fluorides@Reduced Graphene Oxides for Na-Ion Storage with Pseudocapacitive Conversion/Insertion Dual Mechanisms. *Chem. Eur. J.* **2021**, *27*, 9954–9960. [CrossRef]

162. Yan, T.; Ding, R.; Huang, Y.; Ying, D.; Tan, C.; Huang, Y.; Yang, F.; Sun, X.; Gao, P.; Liu, E. A novel sodium-ion supercabattery based on vacancy defective Ni–Co–Mn ternary perovskite fluoride electrode materials. *J. Mater. Chem. A Mater.* **2021**, *9*, 14276. [CrossRef]
163. Yang, F.; Ding, R.; Jia, Z.; Yu, W.; Li, Y.; Wang, A.; Liu, M.; Xie, J.; Yan, M.; Fang, Q.; et al. High specific energy and power sodium-based dual-ion supercabatteries by pseudocapacitive Ni-Zn-Mn ternary perovskite fluorides@reduced graphene oxides anodes with conversion-alloying-intercalation triple mechanisms. *Energy Storage Mater.* **2022**, *53*, 222–237. [CrossRef]
164. Zhu, Y.; Xu, H.; Ma, J.; Chen, P.; Chen, Y. The recent advances of NASICON-$Na_3V_2(PO_4)_3$ cathode materials for sodium-ion batteries. *J. Solid State Chem.* **2023**, *317*, 123669. [CrossRef]
165. Du, G.; Pang, H. Recent advancements in Prussian blue analogues: Preparation and application in batteries. *Energy Storage Mater.* **2021**, *36*, 387–408. [CrossRef]
166. Mao, Y.; Chen, Y.; Qin, J.; Shi, C.; Liu, E.; Zhao, N. Capacitance controlled, hierarchical porous 3D ultra-thin carbon networks reinforced Prussian blue for high performance Na-ion battery cathode. *Nano Energy* **2019**, *58*, 192–201. [CrossRef]
167. Munkalia, S.; Dahal, R.; Kokayi, M.; Jackson, T.; Bastakoti, B.P. Hollow Structured Transition Metal Phosphates and Their Applications. *Chem. Rec.* **2022**, *22*, e20220. [CrossRef] [PubMed]
168. Gabriel, E.; Ma, C.; Graff, K.; Conrado, A.; Hou, D.; Xiong, H. Heterostructure engineering in electrode materials for sodium-ion batteries: Recent progress and perspectives. *eScience* **2023**, *3*, 100139. [CrossRef]
169. Zhang, Y.; Tang, D.; Liu, Y.; Wang, J.; Li, Z.; Li, X.; Han, G.; Wei, Q.; Qu, B. Sodium Stoichiometry Tuning of the Biphasic-Na_xMnO_2 Cathode for High-Performance Sodium-Ion Batteries. *Small* **2023**, *19*, 2301141. [CrossRef]
170. Huang, Z.-X.; Zhang, X.-L.; Zhao, X.-X.; Zhao, Y.-Y.; Aravindan, V.; Liu, Y.-H.; Geng, H.; Wu, X.-L. Electrode/electrolyte additives for practical sodium-ion batteries: A mini review. *Inorg. Chem. Front.* **2023**, *10*, 37–48. [CrossRef]
171. Pérez-Vicente, C.; Medina, A.; Alcántara, R. A Comparative View of Alkaline and Alkaline-Earth Element Intercalation into Perovskite-Type $A_xLa_yTiO_3$ (A = Li, Na, or Mg) Based on Theoretical Calculations and Experiments. *ACS Appl. Energy Mater.* **2022**, *5*, 15749–15757. [CrossRef]
172. Park, H.; Guo, Z.; Manthiram, A. Effect of Oxidative Synthesis Conditions on the Performance of Single-Crystalline $LiMn_{2-x}M_xO_4$ (M = Al, Fe, and Ni) Spinel Cathodes in Lithium-Ion Batteries. *Small* **2023**, 2303526. [CrossRef]
173. Zuo, D.; Yang, L.; Zou, Z.; Li, S.; Feng, Y.; Harris, S.J.; Shi, S.; Wan, J. Ultrafast Synthesis of NASICON Solid Electrolytes for Sodium-Metal Batteries. *Adv. Energy Mater.* **2023**, *13*, 2301540. [CrossRef]